Critical Heat Flux and the Dryout of Liquid Film in Two-phase Annular Flow

by

Roman W. Morse

A thesis submitted in partial fulfillment of
the requirements for the degree of

Master of Science
(Mechanical Engineering)

at the

University of Wisconsin-Madison

2020

Date of defense presentation: 16 December 2020
The thesis is approved by the following members of the Defense Committee:
Greg F. Nellis, Ouweneel-Bascom Professor, Mechanical Engineering
Arganthaël Berson, Lecturer, Mechanical Engineering
Kristofer M. Dressler, Lecturer, Mechanical Engineering

Approved: Greg Nellis

Gregory F. Nellis, Professor of Mechanical Engineering

Abstract

Critical Heat Flux and the Dryout of Liquid Film in Two-phase Annular Flow

Roman W. Morse, Master of Science
Department of Mechanical Engineering
University of Wisconsin-Madison, 2020

Professor Gregory F. Nellis, Advisor
Arganthaël Berson, Co-advisor
Kristofer M. Dressler, Co-advisor

The entire liquid-film dryout process in a vertical two-phase annular flow is characterized experimentally, from inception to completion. Experiments are conducted using saturated R245fa at high vapor qualities in a heated rectangular channel with a hydraulic diameter of 18 mm and an aspect ratio of 1/3. The walls of the test section are made of glass coated with fluorine-doped tin oxide (FTO). Heat fluxes up to 50 kW/m^2 are generated at the inner surface of the window by passing an electrical current through the FTO coating. Instantaneous pressure and temperature in the test section, temperature on the outer wall of the test section, liquid-film thickness, and high-speed videos are recorded simultaneously during the dryout events. In addition, the state (wet or dry) of the heated surface is measured using a non-invasive laser reflectance technique at high sampling rate (2000 Hz) and over long periods of time ($>$ 1000 s). The laser reflectance measurement is used to calculate the time-averaged dry fraction, f_{dry}, which is the fraction of time that the wall is dry during intermittent cycles of dryout and rewet. Data show that cyclic dryout starts before the critical heat flux (CHF) is reached. The dryout heat flux (DHF), which marks the onset of dryout, is typically 90% of the CHF, except at very high quality ($x > 0.95$), where it can be as low as 50% of CHF. For all the investigated mass fluxes, CHF, where the heat transfer coefficient peaks, occurs consistently at $f_{dry} \approx 0.05$.

Further insight into the liquid-film behavior at the onset of dryout is obtained by combining analyses of high-speed videos, time-resolved liquid-film thickness signals, and statistics about the duration of and time between dryout events. The rewetting process is driven by

disturbance waves. In the wake of disturbance waves, the liquid film is almost stationary. Calculations of the characteristic time it takes for this stationary film to evaporate predict well the characteristic time during dryout events measured with the laser reflectance method.

Acknowledgements

I would like to thank my advisors and co-advisors: Greg Nellis, Arganthaël Berson, and Kris Dressler. Thank you Greg, for being a seemingly bottomless pit of knowledge and for your cryocool temperament. Thank you Arganthaël, for your unparalleled attention to detail and your ability to ask thought-provoking questions. Thank you Dressler, for being the glue that holds the lab together, and for being a great teacher, mentor, and friend. Thank you all for believing in my ability to perform as a student, a researcher, and a teacher, and for all of the guidance you have provided throughout the making of this work. You have consistently gone to bat for this guy with tattoos and a top-knot, and for that I am truly grateful.

I would also like to thank colleagues who I have had the opportunity to work with and learn from. Thank you Brian, for greatly improving the facility, spending many hours in the lab together, and most importantly, playing jams. Thank you Jason, for being the technical wizard this facility needs. Thank you Tiago, for your two-phase flow savvy and for introducing us to picanha. Also, thank you to the undergraduates that have spent hours skinning knuckles and mopping up leaks: Sydney, Wausau, Chris, Michael, Jake, and Drew. Without contributions from all of you, this work would not be possible.

I would like to express my extreme gratitude towards my family. Thank you Mama, for all of your support through this thing we call life. Without it, I would still be lost. Thank you Noah and Pups, for keeping me grounded and for always having my back. Thank you to my furry little family, Kylie and Nero, for providing support on a daily basis, and for putting up with me spending countless hours late at night staring at plots, MatLab error messages, and high-speed video. I love and appreciate you all.

Lastly, thank you science, for being so damn awesome.

Contents

List of Figures

Nomenclature

Abbreviations

LR	Laser reflectance
CHF	Critical heat flux
DHF	Dryout heat flux
EES	Engineering Equation Solver
FTO	Fluorine-doped tin oxide
HTC	Heat transfer coefficient
MFVAL	Multiphase Flow Visualization and Analysis Lab

Symbols

δ	Film thickness
δ_{vs}	Thickness of viscous sublayer
$\dot{m}$	Mass flow rate
$\dot{q}$	Heating power
$\dot{q}''$	Heat flux
$\mathcal{H}$	Normalized heat transfer coefficient
μ	Fluid viscosity
ρ	Fluid density
A_c	Test section cross-sectional area
D_h	Hydraulic diameter
f_{dry}	Temporal dry fraction
G	Mass flux

h Local heat transfer coefficient

h_{tp} Maximum local HTC that occurs prior to dryout

i Specific enthalpy

L Length

Nu Nusselt number

P Pressure

R_{ts} Thermal resistance through the sides of the test section

Re Reynolds number

T Temperature

T_{sat} Saturation temperature

T_w Temperature of the interior wall (heated surface) of the test section

x Vapor quality

Subscripts

$crit$ Critical

di Dryout incipience

eff Effective

ext Exterior wall of test section

in Inlet of test section

l Liquid phase

out Inlet of test section

sat Saturation conditions

sc Subcooled conditions

sh Superheated conditions

v Vapor phase

Chapter 1

Introduction

Flow boiling is an effective method for cooling high heat flux devices, such as concentrated solar photovoltaic cells and microprocessors, where a sudden increase in surface temperature can cause damage and possibly the complete failure of the device. In flow boiling, energy is transferred from the walls of a heated channel to a saturated fluid by a combination of forced convection and evaporation. A very important phenomenon that can occur during flow boiling is the onset of the boiling crisis, which is characterized by a severe reduction in heat transfer from the heated surface to the fluid and results in a rise in surface temperature. To prevent such situations, it is important to understand the mechanisms that lead to the boiling crisis.

In flow boiling systems, the saturated fluid progresses through a series of flow regimes as vapor quality is increased. The process is visualized in Figure 1.1. The figure can be interpreted in two ways: (1) heat flux is constant and quality increases along the axis of the channel; or (2) the location is fixed and quality increases with increasing heat flux at the wall. The heat transfer coefficient (HTC) is the proportionality constant that relates the heat flux to the temperature difference between the heated surface and the saturated fluid. In general, HTC increases with increasing vapor quality, and reaches a maximum value in the annular regime (Collier and Thome (1994)), which is the focus of the current study.

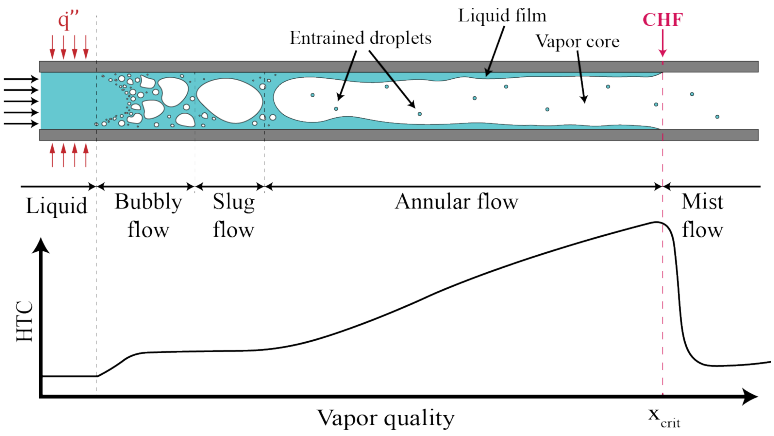

Figure 1.1: Flow boiling regime progression (top) and qualitative description of HTC (bottom). Higher HTC indicates more effective heat transfer. Figure adapted from Kim and Mudawar (2013).

Annular flow is characterized by a vapor core, liquid film on the wall, and liquid droplets entrained within the core. Shear at the liquid-vapor interface drives the flow of the liquid film along the heated surface. In general, the two-phase HTC increases as the liquid-film thickness decreases. For given flow conditions, there exists a combination of heat flux and vapor quality such that the local HTC reaches a maximum. Increasing the heat flux or vapor quality past this critical point results in a reduction in heat transfer coefficient. The reduction in HTC is associated with some degree of liquid-film dryout because the liquid film is depleted and replaced by vapor which has a lower thermal conductivity. The value of the heat flux at which the local maximum in HTC occurs is referred to as the critical heat flux, CHF, and the associated vapor quality is referred to as the critical vapor quality, x_{crit}. The HTC degradation that ensues when heat flux has exceeded the CHF is referred to as the boiling crisis.

It is necessary to define the nomenclature used to describe CHF and dryout because nomenclature in the literature is inconsistent between authors. Table 1.1 contains different definitions for flow boiling CHF provided in the literature. The majority of the descriptions provided for flow boiling CHF in the literature have been qualitative. Only the final two

entries in the table provide quantitative descriptions, neither of which can be used universally. The quantitative definition of CHF used in this current work is consistent with the qualitative description provided by Collier and Thome (1994).

Author & year	**Nomenclature**	**Definition**
Collier and Thome (1994)	Critical heat flux	Heat flux at which, and local to a point, the characteristic reduction in HTC first occurs.
Nellis and Klein (2009)	Critical heat flux	The heat flux at which the burnout point occurs, a small increase in heat flux results in a large increase in excess temperature.
Shah (1987)	Critical heat flux	Exceeding this heat flux results in inefficient heat transfer and can result in the catastrophic failure of device.
Del Col and Bortolin (2012)	Onset of dryout	Temperature fluctuations due to the liquid-film dryout.
Kim and Mudawar (2013)	Critical heat flux	The point at which dryout completion is reached.
Borhani and Thome (2014)	Onset of critical heat flux	At CHF the liquid film covering a heated wall dries out, thus exposing the surface to the vapor flow; resulting in a significant drop in the HTC.
Nascimento et al. (2019)	Critical heat flux	Drastic reduction in HTC associated to the surface dryout, which implies a drastic increase in surface temperature.
Revellin et al. (2008)	Critical heat flux condition	Occurring when the interfacial wave amplitude is equal to the local film thickness, exposing the heated surface to the vapor core.
Wojtan et al. (2006)	Critical heat flux	$CHF = Aq_{max}$, $q_{max} = \rho_v i_{lv}\sqrt{RT/2\pi M}$, where $A = 0.1$ for water, and $A = 0.01$ for refrigerants.
Ong and Thome (2011),Tibiriçá et al. (2012)	Critical heat flux	The heat flux that results in the surface temperature reaching a temperature that is 40 K greater than the saturation temperature.

Table 1.1: Different terms and definitions used to describe CHF in flow boiling

In flow boiling systems, the reduction in HTC and onset of boiling crisis are largely due to one of two mechanisms depending on the flow conditions. For sub-cooled flows and saturated flows at low vapor qualities (bubbly or slug/plug flows) the main heat transfer mechanism is nucleate boiling. In this regime, the boiling crisis occurs when the flow departs from nucleate

boiling (DNB), as vapor bubbles impede the ability of liquid to rewet the surface. Significant progress has been made recently in understanding the mechanisms leading to CHF during nucleate boiling (Galloway and Mudawar (1993)). As a result, better heat transfer surfaces were designed, significantly increasing the value of CHF in this flow regime (Zhang et al. (2012); Ahn et al. (2010)).

At high vapor quality in the annular flow regime, the boiling crisis and reduction in HTC are associated with the loss of liquid film, also known as dryout. Locally, a dryout event occurs when the liquid film ruptures, exposing the heated surface to the vapor core. However, the transition from the annular regime to a mist flow is not sharp. At the location where the liquid film first ruptures, the wall may be subject to intermittent periods of dryout and re-wetting. The dryout process may therefore be characterized by a vapor quality associated with dryout incipience, x_{di}, a vapor quality associated with reaching the CHF x_{crit}, and vapor quality corresponding to the conditions where the liquid film is unable to rewet, x_{dc} (Wojtan et al. (2005); Revellin et al. (2008); Del Col and Bortolin (2012); Marathe and Webb (2008); Kanizawa et al. (2016); Diani et al. (2018); Lillo et al. (2019)). The correct determination of the vapor quality associated with dryout incipience and the vapor quality associated with CHF is important for developing accurate and reliable prediction methods for the two-phase HTC and CHF (Wojtan et al. (2005); Kim and Mudawar (2013); Borhani and Thome (2014); Kanizawa et al. (2016)).

Comparisons of experimental data with predictive correlations for CHF have been extensively performed (Shah (1987); Groeneveld (2012); Ong and Thome (2011);Wojtan et al. (2006); Katto and Ohno (1984); Tibiriçá et al. (2012); Qu and Mudawar (2002); Zhang et al. (2006)). These correlations are not always in agreement. Discrepancies are often due to the differences in the experimental databases from which the correlations are derived. Also, the conditions used to identify the CHF differ depending on the experimental work.

Comparisons of experimental data and correlations provided in the literature for dryout inception vapor quality x_{di} were performed by Kim and Mudawar (2013), Anwar et al.

(2015), Kanizawa et al. (2016), Del Col et al. (2007), Lillo et al. (2019) and Wojtan et al. (2005). Again, each correlation usually works best for a specific experimental database. Kim and Mudawar (2013) highlighted that, besides the authors' own, the prediction method of Mastrullo et al. (2012) also presented reasonable results. Mastrullo et al. (2012) and Kim and Mudawar (2013) prediction methods were also found by Lillo et al. (2019) to be accurate and they highlighted the method of Wojtan et al. (2005) as the most accurate for their database. It is worth highlighting that although some authors found reasonable agreements between the experimental data and correlations, a limited number of studies involving dryout incipience vapor quality are available in the literature. In the case of vertical rectangular channels, the subject of this work, there are no studies in the literature to the authors knowledge.

Within the intermittent dryout region, the liquid film experiences intermittent ruptures leading to dry patches that are periodically rewetted (Borhani and Thome (2014)). For a fixed heat flux, as quality progresses from x_{di} to x_{dc}, these dry patches become larger and rewetting happens less frequently, until the surface remains dry indefinitely ($x \geq x_{dc}$). The oscillatory behavior of dryout was first observed as small fluctuations in the exterior wall temperature, and used as an indication the heat flux was approaching CHF (Collier and Thome (1994);Jabardo and Bandarra-Filho (2000); Del Col and Bortolin (2012);Nascimento et al. (2019)). Recently, Nascimento et al. (2019) recorded an increase in the temperature oscillations when approaching dryout conditions in their microchannel experiment. They ascribed these temperature oscillations to the movement of the fluid front at heat fluxes approaching CHF. However, they were unable to visualize the liquid film during these experiments to confirm their assumptions.

Detailed, time-resolved measurements of two-phase flow during conditions when dryout occurs are rare in the literature. Borhani et al. (2010) gathered high-speed images of intermittent dryout under slug flow inside a multi-microchannel heat exchanger. The authors identified two stages in the dryout mechanism. The first is the dewetting stage, when perturbations in the liquid-film thickness grow to critical amplitudes beyond which the liquid film

ruptures. The second stage is the evaporation stage where the remaining liquid droplets on the heated surface are vaporized. Borhani et al. (2010) observed that in slug flow a region will remain dry until the passage of a liquid slug rewets the surface.

The same authors performed a second study, this time investigating horizontal annular flow during intermittent dryout within a multi-microchannel heat exchanger (Borhani and Thome (2014)). The authors observed that increasing heat flux resulted in an increase in velocity for both the wetting front and the drying front of the liquid film. Borhani and Thome (2014) observed that the liquid film ruptures at a frequency between 40 and 50 Hz, roughly half the frequency of the interfacial waves at the inlet. Droplet deposition, entrainment and bubble nucleation were observed by the authors to occur at frequencies much higher than the rupturing frequency. Also, Borhani and Thome (2014) observed conditions where the local position was dry more than 10% of the time but the temperature remained stable. The authors note that the heat transfer performance may be affected but that the CHF had not yet been reached. Finally, Borhani and Thome (2014) identified two factors impacting local dryout: (1) the behavior of the interfacial waves; and (2) streamwise variation in the liquid-film thickness due to evaporation, droplet entrainment, and droplet deposition. The authors identified the behavior of the interfacial waves to be the most important and least understood mechanism. The authors also present a sheared-film break up model for horizontal flow over an impermeable solid wall by making the analogy to a stationary film. Perturbations along the liquid film change the local thickness. A critical perturbation is one that causes the local liquid film to rupture and the formation of a dry region on the wall. It is calculated using the liquid-solid contact angle and fluid properties.

Mancin et al. (2016) recorded high-speed images of the mechanism in a conventionally sized (hydraulic diameter greater than 3 mm) rectangular channel at high vapor quality annular flow conditions. These authors observed that at the very first moment of the dryout, small regions of the surface dry and rewet intermittently. The area of the dry regions increases with vapor quality, resulting in decreasing HTC, despite intermittent rewetting.

This behavior continues until the amount of liquid in the flow diminishes so much that the rewetting process is no longer capable of reaching the dry zones. At high heat flux, the first stage disappears and the HTC is affected almost instantaneously as dry regions grow rapidly. As heat flux increases, the surface becomes completely dry at lower vapor qualities, i.e., the dryout completion vapor quality decreases with increasing heat flux, which was verified by Lillo et al. (2019). Increasing mass velocity has the opposite effect on the first stage of dryout. At high mass velocity, the liquid film has greater momentum, which promotes rewetting of the intermittent dry regions and helps maintain good heat transfer. As mass velocity increases, the dryout inception vapor quality, x_{di}, increases. These results were corroborated by Diani et al. (2018) for mass fluxes in the range $G < 100$ kg/m^2-s.

As discussed above, only Borhani et al. (2010), Borhani and Thome (2014), and Mancin et al. (2016) performed flow visualizations of the dryout mechanism. None of the previous studies were for vertical rectangular channels, as is the case in the current study. Previous studies capable of visualizing the flow have done so through an unheated surface. Also, there are very few studies available in the literature concerned with the vapor quality at which dryout events first appear. None of the previous studies presented time-resolved film thickness measurements or time-resolved data relating to the dryout phenomenon.

The main goal of the current work is to provide a detailed qualitative and quantitative description of how the flow transitions to the boiling crisis based on local quantities. The dynamic behavior of the liquid film during dryout is characterized directly by combining time-resolved measurements of the liquid-film thickness, the local conditions (wet or dry) of the channel wall, and high-speed imaging of the flow field. The unique breadth of highly time-resolved data included in this report may be useful to guide modeling efforts to predict dryout and CHF in a more robust way.

Chapter 2

Experimental

2.1 Experimental apparatus

In this experiment, a two-phase annular flow with known enthalpy enters a test section with electrically heated walls. A simple thermal resistance model is employed to account for energy losses, allowing for accurate prediction of the amount of energy transferred to the two-phase fluid and enabling calculations of outlet enthalpy and vapor quality.

Figure 2.1 shows a schematic of the experimental annular flow facility. The working fluid in the two-phase annular flow loop is R-245fa (1,1,1,3,3-pentafluoropropane, Honeywell), a low-pressure refrigerant that possesses fluid properties similar to that of high-pressure steam. The fluid is driven through two circuits, one for vapor and the other for liquid, which combine at the inlet of the developing section to create a two-phase annular flow. The fluid within the vapor circuit starts in the storage tank where the pressure (Omega PX409, 0-344.74 kPa) and temperature (Omega Type K) of the fluid are monitored. From the storage tank, the fluid is driven through the loop by a gear pump (Micropump GJ-N27). Upstream of the pump, there is a plate heat exchanger supplied with cold water (T_{cold} = 10 °C) that is used to cool the fluid below the saturation temperature and avoid cavitation in the pump. Downstream of the pump, the fluid passes through a Coriolis flow meter (Micro Motion F025) and an electronic

proportional control valve (Omega ECV-2506-4X). The mass flow rate from the Coriolis flow meter is read into LabView where a PID controller maintains a specified and constant mass flow rate. After the flow meter, the fluid is evaporated and superheated in a plate heat exchanger supplied with hot water ($T_{hot} = 40$ °C) before entering the flow loop at the vapor inlet. Liquid from the storage tank goes through an identical circuit, without a vaporizing heat exchanger. At the mixing tee, the subcooled liquid from the liquid circuit is injected into the flow through small holes in the channel wall to minimize droplet entrainment and induce annular flow, thus reducing the required two-phase flow development length. Temperature (Omega Type K) and pressure (Omega PX409, 0-344.74 kPa) of the liquid and vapor flows are measured at the inlet and again at the outlet of the mixing tee.

Downstream of the mixing tee, the flow channel transitions smoothly from a 1 inch diameter copper pipe to a stainless steel rectangular channel. It is followed by an insulated channel with length 150 times that of the hydraulic diameter, $D_h = 18$ mm to achieve fully developed flow (Zhao et al. (2013)). The test section consists of an Ultem (polyetherimide) plastic frame, aluminum plates and two windows coated with a layer of fluorine-doped tin oxide (FTO) thickness around 450 nm (estimated by the manufacturer). The flow channel cross section is 36 mm x 12 mm and the heated length is equal to the length of the windows, 0.525 m. By passing an electric current through the FTO coating, the inner wall of the test section can be heated. Constant electrical power is supplied to the windows by two 6 kW Xantrex-XDC power supplies. The uniformity of heating at the windows was verified by measuring the temperature field in the absence of flow with an infrared camera.

The bulk fluid temperature within the test section is measured at four locations using Omega Type E thermocouples with a bare junction of 0.076 mm. The thickness of the liquid film is on the order of tens of microns and inherently unstable. It is important that any instrumentation within the test section be installed in such a manner as to minimize disruption to the liquid film. To accomplish this, a volume is hollowed out of the Ultem midsection and a plug is inserted into the volume. The circular plug has a small slit across the diameter

and the thermocouple is placed within the slit. It was verified that the thermocouples do not protrude into the flow channel using calipers. Each of the thermocouples are calibrated using a refrigerated water circulator to an average uncertainty of 0.05 °C. After calibration, it was verified that the thermocouples accurately measure the saturation temperature calculated from the test section absolute pressure sensor.

Pressure drop measurements are made along the test section using a slow but very accurate sensor (Rosemont 3051cd 0-4.982kPa, response time $\sim$ 700 ms and uncertainty of 7 Pa) and also a fast, less accurate model (Omega PX409-2.5DDUI, response time $\sim$ 1 ms and and uncertainty of 70 Pa). A non-invasive optical technique primarily used to measure inner wall temperature (Fehring et al. (2020)) is adapted and used to indicate dryout. High-speed video is taken at the same location as the film thickness using a Phantom V311 high-speed camera at 4000 fps. Using the same camera, a non-invasive optical method is used to measure liquid-film thickness (Hurlburt and Newell (1996); Shedd and Newell (1998);Moreira et al. (2020)) at a frequency of 4000 Hz. The location of these measurements is near the top of the test section. After leaving the heated test section, the fluid enters a separation tank that acts as a buffer and prevents large pressure oscillations in the test section. The fluid condenses in a plate heat exchanger supplied with cold water and then reenters the storage tank.

Temperatures within the loop are controlled with a separate water/glycol loop. A 10 kW heat pump (Trane WPWD07230D22000T) and a 17 kW heat pump (Trane EXWE06011) extract energy from the cold water side and provide it to the hot water side. The heat pumps are controlled via process controllers (OmegaCal9400). The water/glycol mixture from a 189 L cold reservoir is pumped through counter-flow heat exchangers to condense and cool the refrigerant in the two-phase loop. Water/glycol mixture from a 76 L hot side reservoir is pumped through a single counter-flow heat exchanger where the heat vaporizes the refrigerant.

A data acquisition system from National Instruments and a personal computer are used to

control and monitor the experimental apparatus and record the data. This data acquisition system consists of a chassis model cDAQ-9179, a NI-9401 digital module, two NI-9203 current input modules, two NI-9263 voltage output modules, a NI9205 voltage input module, two NI-9213 temperature input modules and a NI-9215 voltage series input module. An interface program was developed in LabVIEW National Instruments (2019) to control and monitor the experimental apparatus and record the data. Process data is sampled at 2000 Hz.

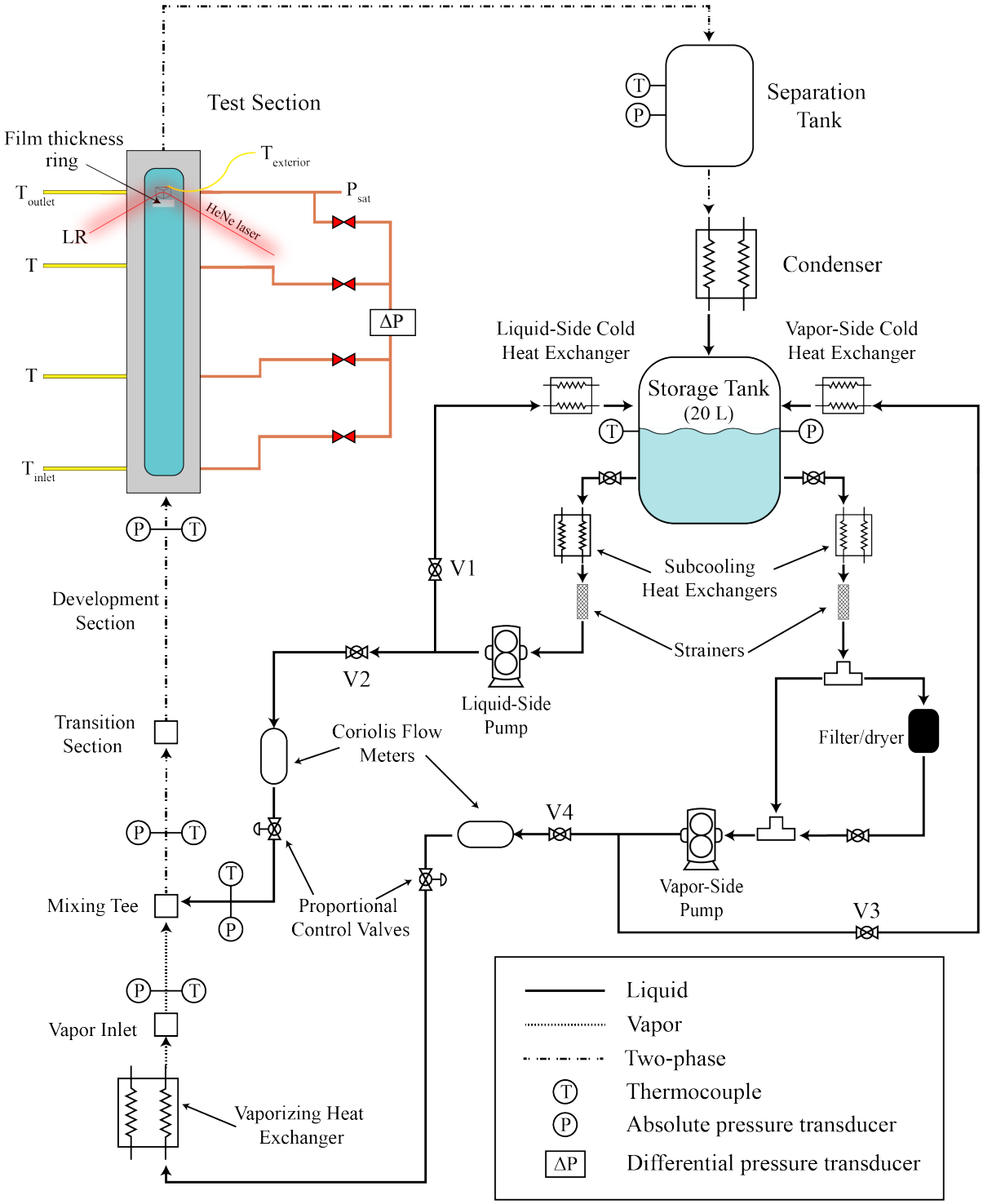

Figure 2.1: Schematic of the R-245fa annular flow loop

2.2 Data regression for process conditions

The goal for the current work is to investigate the flow characteristics that lead to CHF conditions, and also to characterize the behavior of the liquid film during intermittent dryout. A combination of time averaged process data and highly time-resolved data is employed to facilitate this investigation.The experimental apparatus and procedure, are validated by comparing single-phase vapor R245fa data to predictions obtained from correlations in the literature.

2.2.1 Pressure drop

A comparison between experimental and predicted frictional pressure drop is performed for varying vapor mass flow rates in order to verify that the test section used in this study behaves in a manner similar to a conventional smooth channel and check the instrumentation. Under single-phase conditions, the pressure difference measured along the test section is a combination of pressure loss due to friction, the hydrostatic pressure change due to gravity, and the pressure difference associated with changes in momentum. The latter contribution is negligible. As a result, the gravitational pressure drop is subtracted from the total measured pressure difference to obtain the experimental pressure loss due to friction. It was verified that the flow is fully developed by comparing pressure drop measurements along the development section to measurements made along the test section. Therefore, the pressure gradient is assumed to be constant along the test section.From the pressure gradient and the absolute pressure measured at the outlet of the test section, the pressure at any point within the test section can be inferred and is used to calculate local fluid properties. All fluid properties of R245fa were calculated using EES (Klein (2019)).

The experimental friction factor is calculated from the measured frictional pressure drop

between two ports along the test section. It is given by

$$f_{exp} = \frac{\Delta P_{exp}}{L} \frac{2D_h}{\rho_v u^2} \ , \tag{2.1}$$

where ΔP_{exp} is the measured frictional pressure drop, D_h is the hydraulic diameter, ρ_v is the density of vapor R245fa, and L is the distance between the high pressure and low pressure ports. The mean velocity, u, of the flow is

$$u = \frac{\dot{m}_v}{\rho_v A_c} \ , \tag{2.2}$$

where $\dot{m}_v$ is the measured mass flow rate of the vapor refrigerant, and A_c is the cross sectional area of the test section. The Reynolds number of the single-phase vapor is calculated by

$$\mathrm{Re} = \frac{\rho_v u D_h}{\mu_v} \ , \tag{2.3}$$

where μ_v is the viscosity of the vapor.

The experimental friction factor is shown in Figure 2.2 as a function of the vapor Reynolds number. The friction factor behaves as expected and agrees with the correlations for flow inside of a smooth channel by Blasius (1913), Colebrook (1939), and Petukhov (1970). The external flow correlation of Blasius (1913) tends to slightly underestimate the experimental friction factor, which is to be expected. The internal flow correlations of both Colebrook (1939) and Petukhov (1970) provide accurate estimates of the measured values. The fact that the experimental data agrees with well-established correlations provides confidence that the experimental test section behaves as a conventional flow channel and that mass flow rate, temperature, pressure, and pressure drop are all accurately measured within the facility.

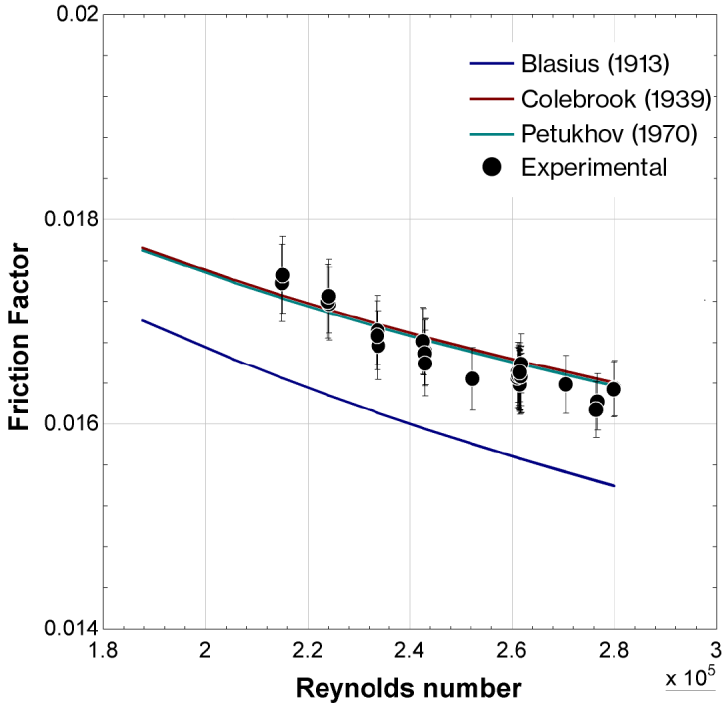

Figure 2.2: Friction factor for single-phase vapor refrigerant as a function of Reynolds number

2.2.2 Calculation of effective heat input

An energy balance in single-phase vapor R245fa is used to characterize heat losses from the test section, which is necessary to calculate the effective heat input into the refrigerant. Heat is generated at the inner wall of the channel by applying electrical power, $\dot{q}_{applied}$, across the FTO coating on the inner wall of the test section. The applied power is calculated with Ohm's law using real-time measurements of the voltage and current in the circuit (accounting for voltage drop across connectors). Only a portion of the applied power is transferred to the refrigerant and the rest is lost to the surroundings. The heat input to the refrigerant is measured using an energy balance on the fluid in single-phase conditions. Pressure and temperature of the superheated vapor are measured at the inlet and outlet of the test section to determine the local specific enthalpies. The measured energy transferred

to the fluid, $\dot{q}_{measured}$, is given by

$$\dot{q}_{measured} = \dot{m}(i_{v,sh,out} - i_{v,sh,in}) \ , \tag{2.4}$$

where $i_{v,sh,in}$ and $i_{v,sh,out}$ are the specific enthalpies of superheated vapor at the inlet and outlet respectively. The heating power lost to the surroundings is calculated as the difference between the applied heating power and the measured change in fluid enthalpy,

$$\dot{q}_{loss} = \dot{q}_{applied} - \dot{q}_{measured}. \tag{2.5}$$

Heat in the test section is lost by conduction through the window and natural convection to the surroundings, and by conduction through the Ultem sidewalls and then natural convection to the surroundings. A thermal network analysis is used to identify the thermal resistances associated with these two pathways, illustrated in Figure 2.3. These resistances can later be used to calculate heat loss in two-phase flow conditions where the local enthalpy measurements are not possible.

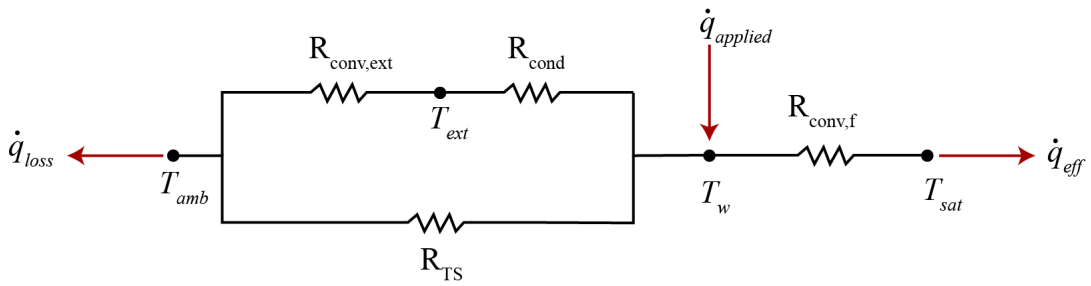

Figure 2.3: Schematic illustrating the thermal resistance network associated with the test section heating apparatus.

The heat loss is given by

$$\dot{q}_{loss} = \overline{h}_{ext} A_{\mathrm{TS}} \left(T_{ext} - T_{amb}\right) + \frac{T_w - T_{amb}}{R_{\mathrm{TS}}} \ , \tag{2.6}$$

where T_{ext} is the temperature of the outer wall in contact with the surroundings, $\overline{h}_{ext}$ is

the heat transfer coefficient associated with natural convection on the exterior of the test section, and R_{TS} is the combined thermal resistance associated with conduction through the Ultem and natural convection to the surroundings. Values of $\overline{h}_{ext}$ = 10 W/m^2-K and R_{TS} = 0.95 K/W were obtained through regression of the data. The effect of temperature on both $\overline{h}_{ext}$ and R_{TS} was found to be negligible. The inner wall temperature, T_w, is calculated by setting the steady-state conduction through the window equal to the energy released by natural convection so that

$$T_w = (T_{ext} - T_{amb}) \frac{\overline{h}_{ext} th_g}{k_g} + T_{ext} \ , \tag{2.7}$$

where k_g = 1.2 W/m-K is the thermal conductivity of glass, and th_g = 3.0 mm is the thickness of the glass wall. The effective heat input, $\dot{q}_{eff}$, is obtained from

$$\dot{q}_{eff} = \dot{q}_{applied} - \dot{q}_{loss} = I\Delta V - \dot{q}_{loss} \ , \tag{2.8}$$

where I is electrical current, ΔV is the voltage potential across the FTO coating, and $\dot{q}_{loss}$ is obtained from Equation 2.6. The effective heating power divided by the surface area of the heated section gives the effective heat flux, $\dot{q}''_{eff}$, received by the fluid at the wall-fluid interface. The heat transfer coefficient for vapor R245fa at the inner surface of the channel is calculated using Equation 2.9,

$$h_v = \frac{\dot{q}''_{eff}}{T_w - T_\infty} \ , \tag{2.9}$$

where T_∞ is the mean bulk fluid temperature measured from the test section outlet thermocouple. The experimental Nusselt number for single-phase vapor R245fa is calculated from the single-phase heat transfer coefficient:

$$\mathrm{Nu} = \frac{h_v D_h}{k_v} \ , \tag{2.10}$$

where k_v is the thermal conductivity of vapor R245fa.

The experimental Nusselt number is compared with predictions from two well-established correlations from the literature by Gnielinski (1975) and by Dittus and Boelter (1930), shown in Figure 2.4. The experimental Nusselt number is shown as a function of the single-phase Reynolds number defined by Equation 2.3. Agreement between the experimental data and both correlations provide confidence in our ability to accurately predict the heat input to the fluid within the test section as well as the performance of the instrumentation required by these tests.

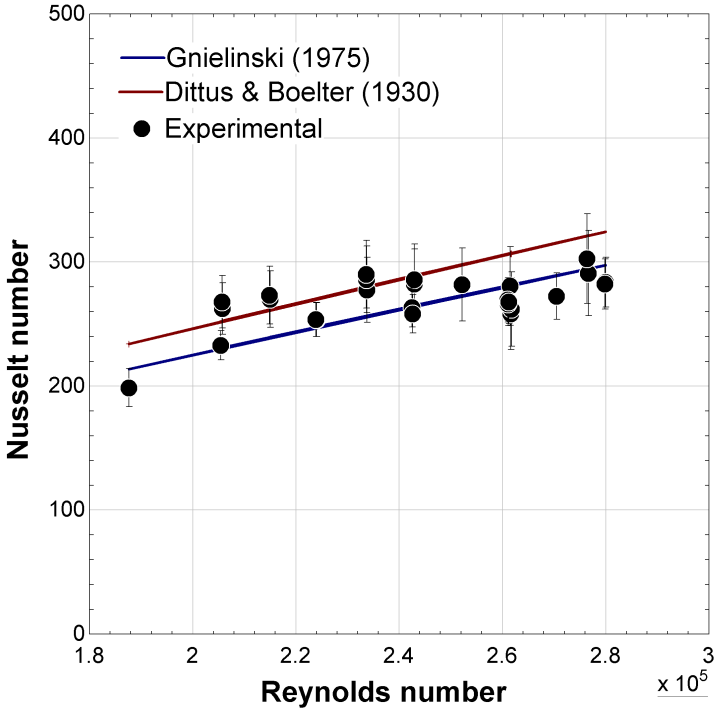

Figure 2.4: Nusselt number for heat transfer to the single-phase vapor refrigerant as a function of Reynolds number

2.2.3 Two-phase calculations

For two-phase flow conditions, an energy balance is performed on the mixing tee to determine the specific enthalpy of the saturated mixture, i_{tp}. The enthalpies of both the slightly superheated vapor phase, $i_{v,sh}$, and slightly subcooled liquid phase, $i_{l,sc}$, are known through measurements of temperature and pressure prior to the two-phase mixing tee. The

enthalpy of the two-phase fluid that exits the mixing tee is given by

$$i_{tp,in} = \frac{\dot{m}_v i_{v,sh} + \dot{m}_l i_{l,sc}}{\dot{m}_v + \dot{m}_l} \ , \tag{2.11}$$

where $\dot{m}_v$ and $\dot{m}_l$ are the vapor and liquid mass flow rates, respectively. The development section immediately following the mixing tee is well insulated and the two-phase mixture is near ambient temperature. It has been verified through an energy balance on single-phase flow that the heat losses through this section are negligible. Therefore the enthalpy of the fluid entering the test section is equal to that leaving the mixing tee. The vapor quality at the inlet of the test section is calculated as

$$x_{in} = \frac{i_{\text{tp,in}} - i_{l,sat,in}}{i_{v,sat,in} - i_{l,sat,in}} \ , \tag{2.12}$$

where $i_{v,sat,in}$ and $i_{l,sat,in}$ are the enthalpies of saturated vapor and liquid, respectively, evaluated at the saturation pressure at the inlet of the test section. The enthalpy of the two-phase fluid at the outlet of the test section is calculated with an energy balance on the fluid moving through the test section:

$$i_{\text{tp,out}} = i_{\text{tp,in}} + \frac{\dot{q}_{eff}}{\dot{m}_v + \dot{m}_l} \ , \tag{2.13}$$

and the outlet vapor quality is given by

$$x_{out} = \frac{i_{\text{tp,out}} - i_{l,sat,out}}{i_{v,sat,out} - i_{l,sat,out}} \ , \tag{2.14}$$

where the enthalpies $i_{v,sat,out}$ and $i_{l,sat,out}$ are the enthalpies of saturated vapor and liquid, respectively, evaluated at the pressure measured at the outlet of the test section.

The experimentally measured local heat transfer coefficient, h, is given by

$$h = \frac{\dot{q}''_{eff}}{T_w - T_{sat}} \ , \tag{2.15}$$

where T_w is calculated using Equation 2.7.

2.3 Uncertainty of measurements

Temperature measurements were calibrated and their uncertainties evaluated according to the procedure suggested by Abernethy and Thompson (1973). The manufacturer's uncertainties of the pressure transducers, power supplies and mass flow meters were adopted. For a given calculated parameter, the uncertainty was estimated accounting for the error of the instruments and measurement procedures using the method of sequential perturbation as proposed by Taylor and Kuyatt (1994). The experimental uncertainties associated with the sensors, estimation procedures and calculated parameters are given in Table 2.1. It is worth highlighting that there are different values of uncertainty for the absolute value of vapor quality, x, and changes in vapor quality δx. The uncertainty of the effective heat flux ($\dot{q}''_{eff}$) has contributions from the uncertainty associated with the power supply and the uncertainty associated with heat losses. The uncertainty for the power supply is provided from the manufacturer. The uncertainty in heat losses is primarily due to the uncertainty in the regressed variables. However, under two-phase flow conditions, approximately 99% of the supplied heat is transferred to the refrigerant. The uncertainty in $\dot{q}''_{eff}$ in Table 2.1 is listed for two-phase flow conditions and therefore is very small.

Parameter	**Symbol**	**Uncertainty**
Absolute pressure	P	300 Pa
Differential pressure	ΔP	7 Pa
Mass flux	G	0.7%
Temperature	T	0.05 °C
Supplied heating power	$\dot{q}_{applied}$	6 W
Heat losses	$\dot{q}_{losses}$	10%
Effective heat flux	$\dot{q}''_{eff}$	0.5%
Heat transfer coefficient	h	1.5%
Local vapor quality	x	0.003
Change in vapor quality	δx	0.0005

Table 2.1: Uncertainties of process measurements

2.4 Time-resolved measurements

2.4.1 Methodology for detection of dryout

The loss of liquid film at the wall is detected in several ways. The first and most obvious method is the use of images from the high-speed videos. Image analysis allows for visualization of the dryout and rewetting process with good time-resolution. However, recording high speed videos is challenging because the duration is limited by the camera memory. Thus, it is difficult to resolve dryout events occurring in a fraction of a second and dryout periods lasting several minutes. In addition, many events must be recorded to obtain meaningful statistics.

A laser reflectance technique is therefore preferred for indication of a dryout event. Although it gives only local information about the state of the wall (wet or dry), it can record data at high speed over very long periods of time (the data sets used in this study range between 15 and 20 minutes). The laser reflectance is derived from an optical technique used to measure temperature within our facility (Fehring et al. (2020)). A laser beam is directed to the glass wall of the test section. At the glass/fluid interface a portion of the beam is reflected and the rest is transmitted into the refrigerant. After passing through a prism and a mirror, the intensity of the reflected beam is measured by a photodiode (Thorlabs PDA55). The ratio of the intensity of the reflected beam to the intensity of the incident laser beam is referred to here as the intensity ratio. The difference in index of refraction between liquid and vapor R245fa is such that, with the appropriate incidence angle, most of an incident laser beam is transmitted into the liquid film whereas most of the light is reflected when vapor is in contact with the window. This leads to a large change in intensity ratio when the wall transitions from wet to dry, as seen in Figure 2.5, during intermittent dryout events.

The laser reflectance measurement location is 1 cm upstream from the exterior thermocouple and 2 cm downstream from the location where film thickness and high-speed video is taken. With this instantaneous indication of wet or dry conditions, a temporally averaged

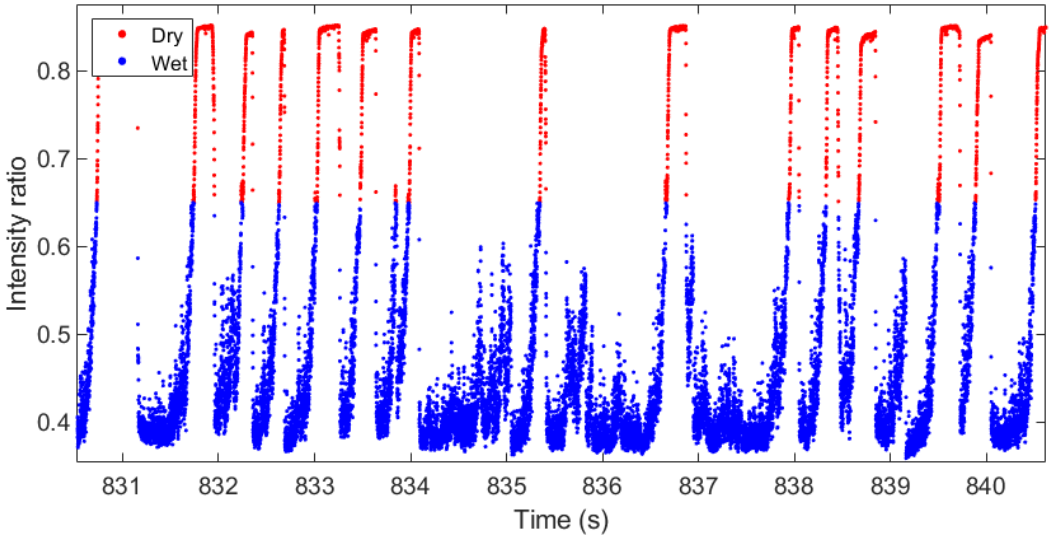

Figure 2.5: Time trace of the intensity ratio signal during dryout events.

dry time fraction f_{dry} can be calculated,

$$f_{dry} = \frac{\text{Cumulative dry time}}{\text{Total time}}. \tag{2.16}$$

The extent of individual dryout events and time between dryout events is also easily recorded using the intensity ratio signal. The uncertainty of f_{dry} is taken as the time it takes for the signal to change from fully wet to fully dry, multiplied by the number of dryout events and divided by the total time. The uncertainty was found to be on average 0.4%.

2.4.2 High-speed video and liquid-film thickness

High-speed video of the liquid film is captured through the transparent test section using a Phantom V311 high-speed camera. The images are acquired at a frame rate of 4000 Hz. In addition, liquid-film thickness is measured during cycles of intermittent dryout-rewet using a non-invasive optical technique (Shedd and Newell (1998); Hurlburt and Newell (1996); Moreira et al. (2020)). The film thickness data are also acquired at a rate of 4000 Hz. The uncertainty in the liquid-film thickness measurement is taken as 8.6 μm, which was shown

through previous work in this facility (Moreira et al. (2020)) to be the maximum uncertainty in the film thickness measurements.

2.5 Two-phase experimental procedure

Figure 2.6 shows an example of time traces of the signals used to identify dryout characteristics of the flow within the test section. The black line represents the effective heat flux applied to the window, $\dot{q}''_{eff}$, the red line represents the exterior wall temperature, T_{ext}, and the blue line represents the local saturation temperature, T_{sat}. Finally, the orange data is the intensity ratio from the laser reflectance measurement.

Prior to collecting data, the flow loop is allowed to reach steady state conditions without any heat input to the test section. In the case of the data set shown in Figure 2.6, heating begins around a time of $t = 80$ seconds after the data acquisition begins. This is shown as a step increase in effective heat flux. After a few seconds, the exterior temperature of the wall reaches a new equilibrium temperature. If the exterior temperature remains constant for a significant amount (greater than 5 times the time-constant for the window) it is assumed the local position has reached a new steady state. At this point, the heating power is increased. At approximately 550 seconds, the first indication of a dryout event occurs in the test section. As heating power is increased further, more dryout events are detected between 650 and 675 seconds. The presence of dryout events can be seen more clearly in the close-ups of the time trace. Figure 2.7 provides three zoomed-in segments corresponding to the dotted boxes labeled as 'Detail 1', 'Detail 2', and 'Detail 3' in Figure 2.6. In Figure 2.7a, for a fixed effective heat flux of 18 kW/m^2, the temperature of the exterior wall remains constant which indicates that the time-averaged heat transfer coefficient at the wall is largely unaffected by these first dryout events. In Figure 2.7b, the effective heat flux is increased to 19.6 kW/m^2, which has caused an increase in frequency and duration of dryout events. The exterior wall temperature increases slightly, about 1 °C, and then reaches a new equilibrium temperature.

The effective heat flux is increased to 21 kW/m^2 at approximately 765 seconds, causing many more dryout events and causing the outer wall temperature to rise 5 °C, corresponding to the first significant reduction in time-averaged heat transfer coefficient. Dryout events occur more frequently and the spacing between events decreases. Finally, at approximately 850 seconds the supplied heat flux is increased to 22 kW/m^2 (an increase of less than 5%), this small increase in heating power results in a large reduction in heat transfer coefficient which is seen in the runaway temperature conditions in Figure 2.7c. This behavior is consistent with boiling crisis conditions resulting from exceeding the CHF. At this point, the experiment is concluded before the window temperature reaches a level that could damage the apparatus.

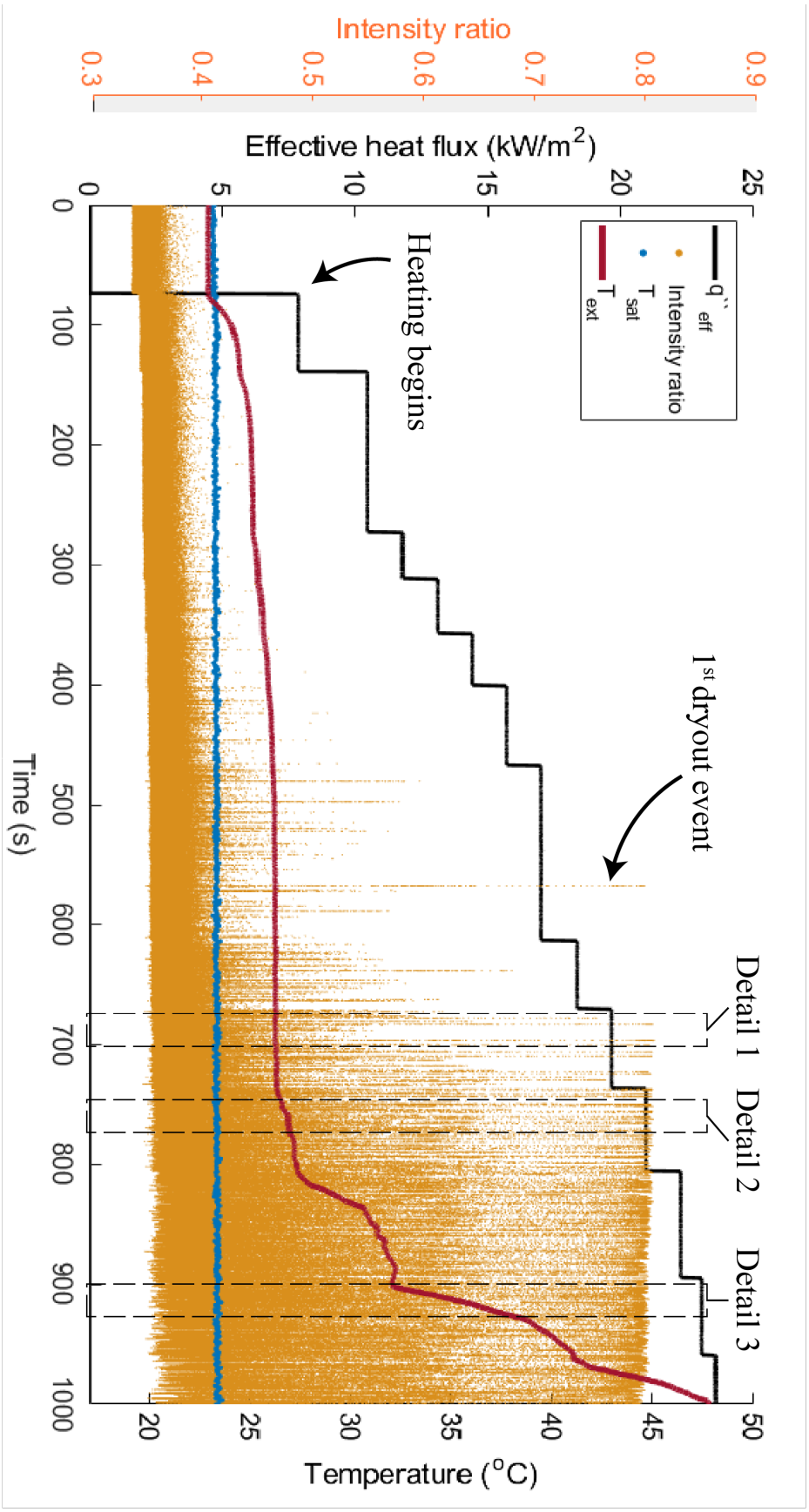

Figure 2.6: Example of data time trace

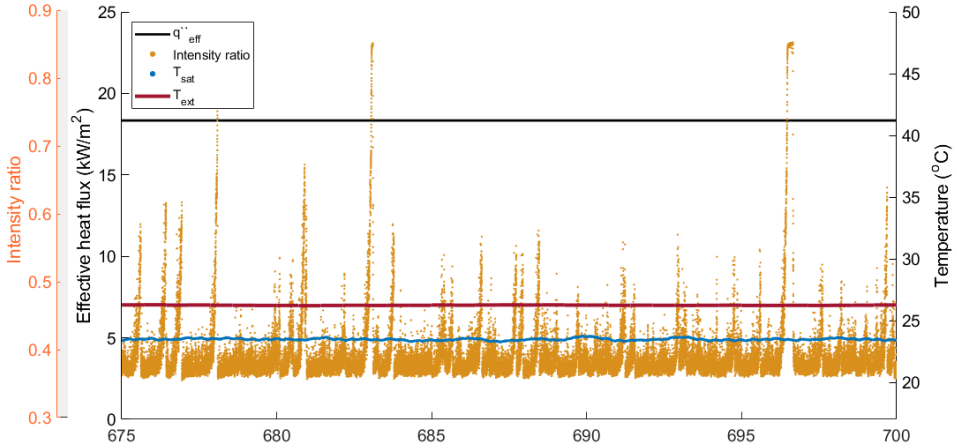

(a) Detail 1

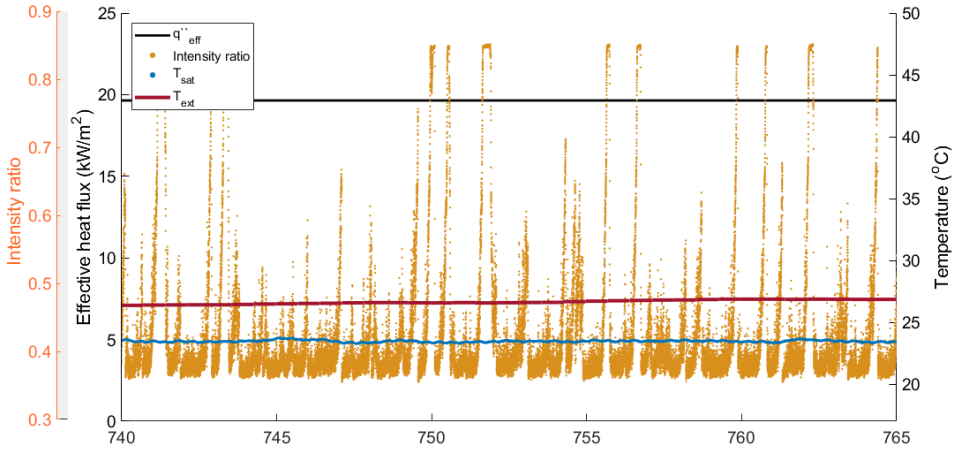

(b) Detail 2

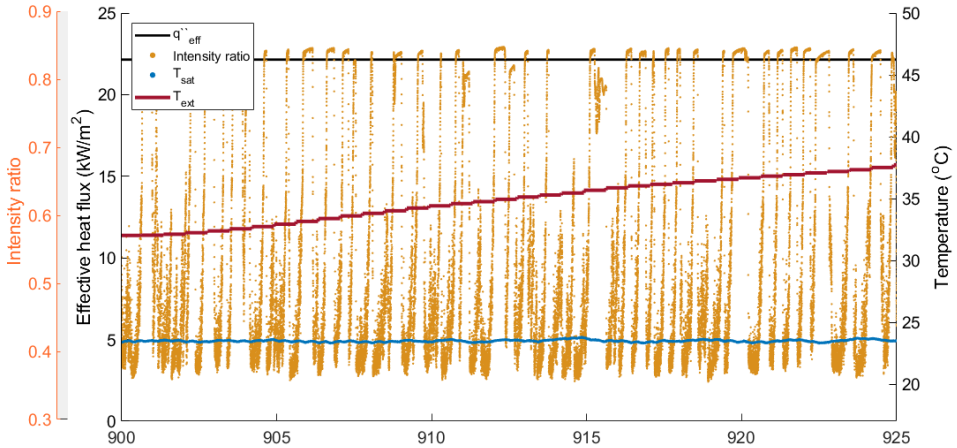

(c) Detail 3

Figure 2.7: Zoomed-in segments of the time traces shown in Figure 2.6.

Chapter 3

Results

This section first presents the experimental values for critical flow conditions; this type of data has been presented by other authors (Ong and Thome (2011), Shah (1987), Wojtan et al. (2006), Katto and Ohno (1984), Tibiriçá et al. (2012), Qu and Mudawar (2002) and Zhang et al. (2006)). The latter part of this section includes dryout event statistics and film thickness measurements capturing dryout events which are not available elsewhere. All of the experimental results were obtained using saturated R245fa as the working fluid. The effective heat flux was varied between 0-40 kW/m^2. The range of mass flux was between 110-170 kg/m^2-s and the range of vapor quality was from 0.7 to 1. The experimental conditions are summarized in 3.1.

Parameter	**Symbol**	**Range**
Effective heat flux	$\dot{q}''_{eff}$	0 - 40 kW/m^2
Mass flux	G	110 -170 kg/m^2-s
Local vapor quality	x	0.7 - 1.0

Table 3.1: Range of experimental conditions

3.1 Onset of boiling crisis

The onset of dryout happens before the start of the boiling crisis. In Figure 3.1, the local heat transfer coefficient and temporal dry fraction are shown as a function of local vapor quality. Initially, as the vapor quality increases there is no change in the local HTC. The measured temporal dry fraction is zero at low vapor qualities and therefore not shown on the figure. At the vapor qualities for which dryout events are first recorded by the intensity ratio signal, the measured HTC increases and reaches a local maximum; this is shown in Figure 3.1 as the blue region labeled 'Intermittent Dryout'. The local maximum in HTC indicates the critical flow conditions. The local values of the local values of $\dot{q}''_{eff}$ and x, are the experimental values of the CHF and x_{crit}, respectively. A further increase in the vapor quality results in the dry fraction increasing to approximately 10% and the first reduction in heat transfer, shown as the first data point within the red region labeled 'Boiling Crisis' on Figure 3.1. Further increase in the vapor quality leads to a large reduction in heat transfer coefficient and a continued increase in the dry fraction. The characteristics of this data set are representative of all the data collected in this work (see Appendix A).

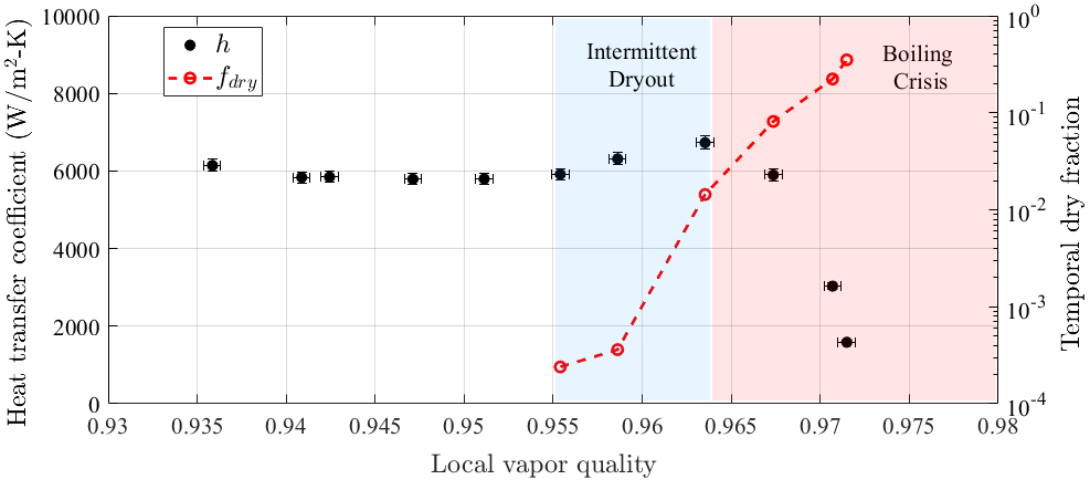

Figure 3.1: Heat transfer coefficient and dry fraction as a function of local vapor quality for data shown in Figure 2.6.

In the following sections, we will investigate in detail the transition to the boiling crisis

by providing qualitative and quantitative descriptions of the flow during the 'Intermittent Dryout' regime.

3.2 Critical flow conditions

First, experimental data for critical heat flux is shown as a function of local vapor quality for mass flux values of 130, 150, and 170 kg/m^2-s in Figure 3.2. For the mass fluxes investigated in this work, there was no significant effect of the mass flux on the value of CHF. As previously stated, the effect of increasing mass flux changes between flows with low mass flux (< 100 kg/m^2-s) and flows with mass fluxes higher than 200 kg/m^2-s. For this reason, the negligible effect of mass flux within this range is expected. The predictions from correlations of Ong and Thome (2011), Shah (1987), and Wojtan et al. (2006) are included in Figure 3.2. The correlation contours were calculated based on the average mass flux associated with the experimental data shown, $G = 150$ kg/m^2-s. A change in slope occurs at relatively high vapor qualities, suggesting a change in regime. The change in slope is captured by the correlations but is most obvious in that of Ong and Thome (2011).

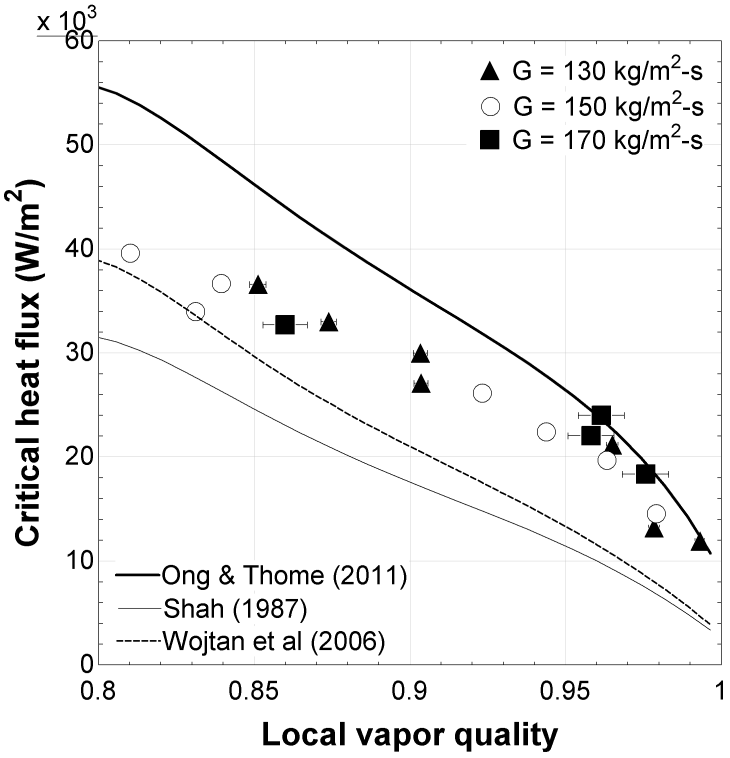

Figure 3.2: CHF as a function of local vapor quality with correlations overlayed

3.2.1 Comparisons to correlations in the literature

Comparison between experimental data for CHF and predicted values from correlations found in the literature is shown in Figure 3.3a. The correlations investigated in this study include Ong and Thome (2011), Shah (1987), Wojtan et al. (2006), Katto and Ohno (1984), Tibiriçá et al. (2012), Qu and Mudawar (2002), and Zhang et al. (2006). Values of CHF predicted by Ong and Thome (2011), Wojtan et al. (2006), and Shah (1987) produced the best agreement with the experimental results. The correlations of Ong and Thome (2011) and Wojtan et al. (2006) were developed using data for two-phase refrigerant flows in a horizontal channel. The correlation of Shah (1987) was developed using a database containing a wide range of fluids, including refrigerants, and vertical channels.

Experimental values for critical vapor quality, x_{crit}, were taken to be the local vapor quality at which the CHF was achieved. The comparison between the experimental values

and those predicted by correlations is shown in Figure 3.3b. The correlations of Mori et al. (2000) and Wojtan et al. (2005) are comparable to one another. and both provide estimates for the experimental value within ±15% error. However, at relatively high heat flux and low vapor quality conditions, both models overestimate the experimental value measured for x_{crit}. Also, at relatively low heat flux and high vapor quality conditions, both models slightly under estimate the measured x_{crit}. The correlations of Kim and Mudawar (2013) and Mastrullo et al. (2012) best capture the data trend, but provide estimates that are consistently lower than the experimentally measured values. The database that Kim and Mudawar (2013) used contains many fluids and flow orientations, but no studies considering vertical flow through rectangular channels are included in the database. This is one possible reason for the error. The correlation of Mastrullo et al. (2012) is developed for horizontal flows, which is likely a factor in why the predictions are different than the experimentally measured values.

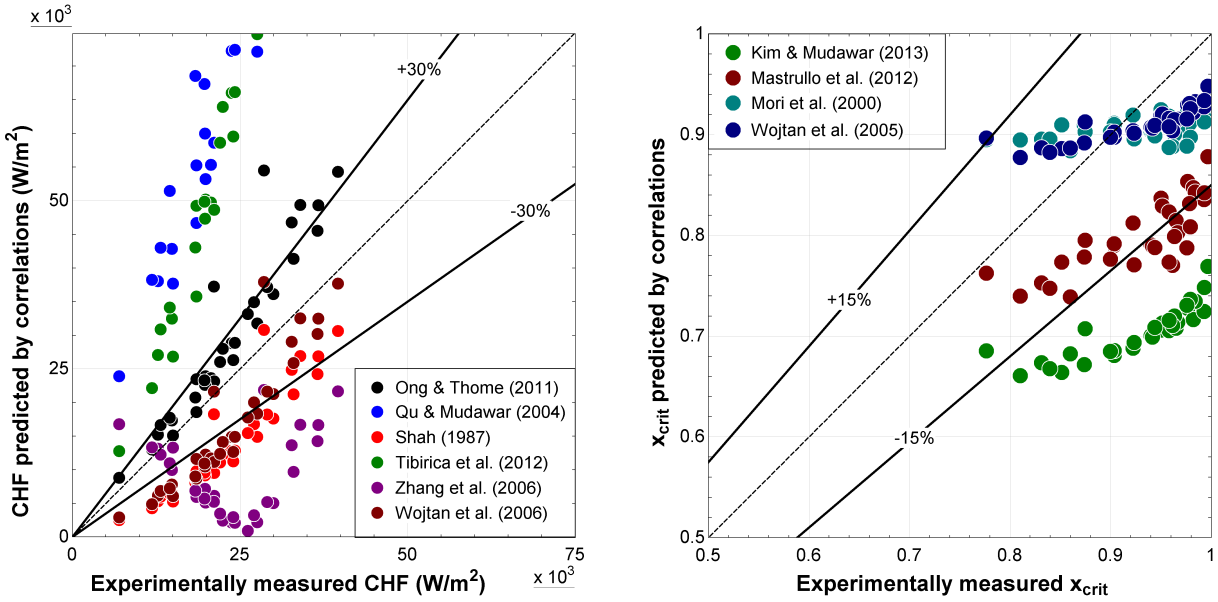

(a) Critical heat flux

(b) Critical vapor quality

Figure 3.3: Comparisons between measured values and predictions from correlations for (a) CHF and (b) x_{crit}.

The lack of good agreement between the different correlations in the literature demon-

strates the need for a more detailed description of the boiling crisis phenomenon, based on local, time-resolved measurements.

3.3 Dryout heat flux and critical heat flux

It was shown earlier in this work that dryout events occur prior to a decrease in heat transfer and therefore prior to the CHF. This was also the observation made by Borhani et al. (2010), Borhani and Thome (2014), and Mancin et al. (2016). The effective heat flux, $\dot{q}''_{eff}$, at which dryout events first occur is referred to as the dryout heat flux (DHF). This section investigates whether DHF can be predicted from knowledge of the CHF. Experimental values of DHF and CHF for a mass flux of $G = 150$ kg/m^{2}s are both shown in Figure 3.4. The red and black dotted lines have been drawn for a visual guide. The local vapor quality associated with the DHF is the dryout incipience vapor quality, x_{di}, and the vapor quality associated with CHF is the critical vapor quality, x_{crit}. Intermittent dryout occurs without a reduction in HTC between the black (DHF) and red (CHF) dotted lines. The slope of the DHF is similar to that of the CHF and also displays a change in slope at high vapor qualities. Referring back to Table 2.1, the uncertainty associated with these measurements are very small.

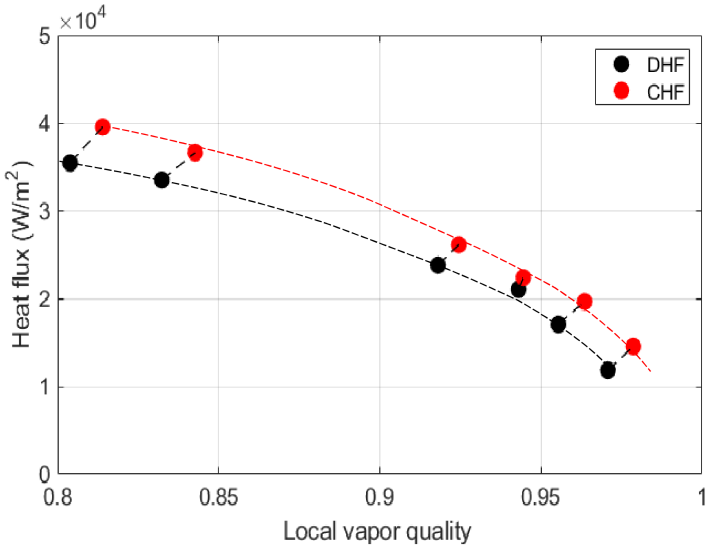

Figure 3.4: Dryout heat flux (DHF) and critical heat flux (CHF) measured at mass flux of G = 150 kg/m^2-s.

Figure 3.5a shows the percent difference between DHF and CHF as a function of CHF. On average, the value of CHF was 10% greater than the value of DHF. However, for low CHF conditions (high vapor quality) dryout begins to occur when $\dot{q}''_{eff}$ is only half the value of the CHF. In Figure 3.5b, the percent difference between x_{di} and x_{crit} is plotted as a function x_{crit}. The percent difference in vapor quality between onset of dryout conditions and critical conditions was found to be small, on average about 1.0%.

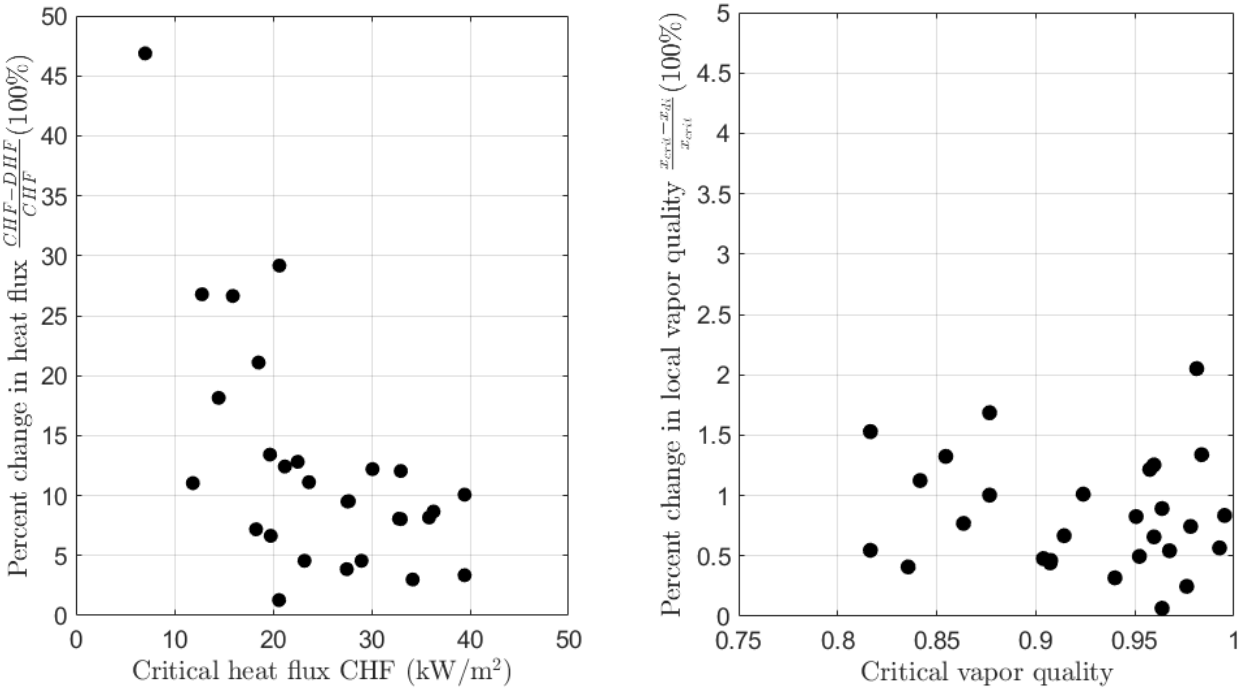

(a) Critical heat flux

(b) Critical vapor quality

Figure 3.5: Dryout conditions and critical conditions for heat flux (left) and vapor quality (right)

3.4 Behavior of HTC for varying dry time

This section aims at characterizing how the local time-averaged HTC, h, behaves for varying temporal dry fractions, f_{dry}. The maximum measured HTC prior to the occurrence dryout events, h_{tp}, and the single-phase vapor HTC, h_v, both increase with increasing mass flux. In an effort to compare data for varying mass flux, a time-averaged HTC normalized heat transfer coefficient, $\mathcal{H}$, is calculated as,

$$\mathcal{H} = \frac{h - h_v}{h_{tp} - h_v} \,, \tag{3.1}$$

where h is the measured time-averaged HTC. It was shown previously in this work that the correlation of Dittus and Boelter (1930) was capable of providing accurate estimates for h_v. A normalized HTC, $\mathcal{H}_{weighted}$, based on simply weighting h_v by the dry time and h_{tp} by the

wet time is calculated as,

$$\mathcal{H}_{weighted} = 1 - f_{dry} \ . \tag{3.2}$$

The normalized HTC and normalized weighted HTC are shown as a function of dry time fraction in Figure 3.6. The weighted average approach fails to predict the HTC in the 'intermittent dryout' regime. With increasing mass flux, the maximum value of $\mathcal{H}$ tends to decrease slightly. Otherwise, for the range of mass fluxes investigated, there is little effect of the mass flux on $\mathcal{H}$ during intermittent dryout. At $f_{dry} \approx 0.05$, the value of $\mathcal{H}$ has increased by approximately 10-25% compared to its initial value prior to any dryout events. The local maximum in $\mathcal{H}$ at $f_{dry} \approx 0.05$ provides the flow conditions in which $\dot{q}''_{eff}$ has reached the CHF. Further into the boiling crisis, the value of $\mathcal{H}$ approaches zero as the HTC approaches the value for single-phase vapor.

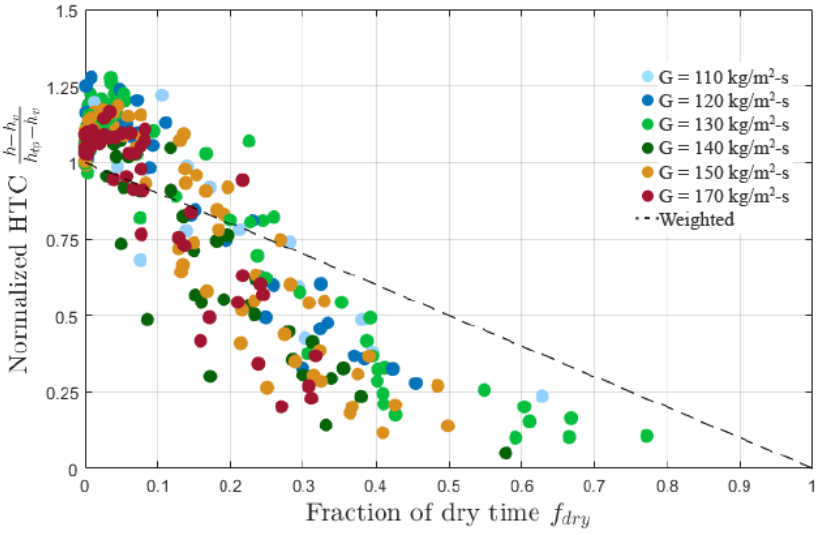

Figure 3.6: Normalized HTC as a function of time-averaged dry fraction.

In Figure 3.7, the same data are shown without differentiating between mass fluxes and on a logarithmic scale. For the conditions at which dryout events are first observed ($f_{dry} < 0.001$), there is no obvious change in the value of $\mathcal{H}$. For $f_{dry} > 0.1$, there is a significant decrease in $\mathcal{H}$ for increasing values of f_{dry}. Between $0.001 < f_{dry} < 0.05$, there is an increase

in the value of $\mathcal{H}$ with increasing f_{dry}.

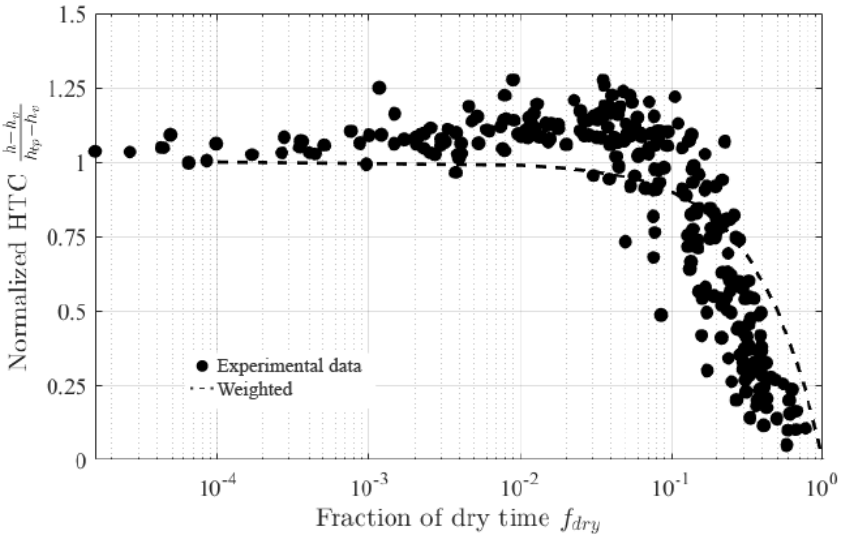

Figure 3.7: Normalized heat transfer coefficient as a function of dry fraction for all mass fluxes

3.5 Liquid film behavior during intermittent dryout

In order to get further insight into the mechanisms of dryout, time-resolved measurements of the liquid-film thickness are analyzed simultaneous with the laser-reflectance data. In this section, experimental data for liquid-film thickness is shown for heated conditions and with constant mass flux of $G = 167$ kg/m^2-s. Figure 3.8 shows a qualitative description of the relationship between CHF and vapor quality, corresponding to experimental data shown in Figure 3.2. The different regimes indicated as 1, 2, and 3 on the figure correspond to the flow regime of the experimental data shown in Figures 3.9, 3.10, and 3.11, respectively.

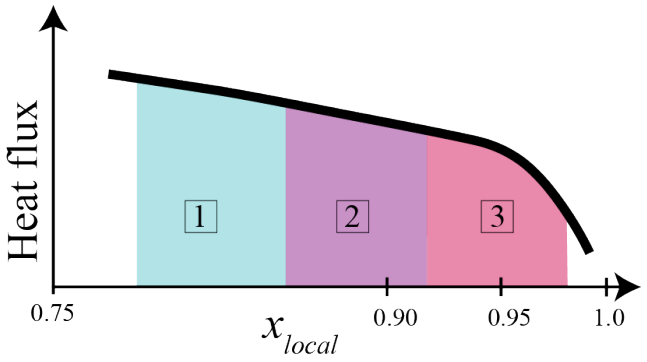

Figure 3.8: Visualization of the flow regimes captured in Figures 3.9, 3.10, and 3.11

Figures 3.9, 3.10, and 3.11 display time traces for flow conditions and the laser reflectance signal (top) in the same manner as shown previously in Figure 2.6. The subfigures are snapshots of film thickness data, each around 2.5 seconds long, taken within the longer data set. The temporal location of each film thickness measurement is indicated with a vertical black dotted line.

3.5.1 Regime 1

The flow conditions corresponding to the first regime are low values of x_{crit} and high values of CHF, with respect to the ranges investigated in this study. Figure 3.9a displays the film thickness in unheated conditions. The large variance in film thickness captures the passage of disturbance waves at a relatively high frequency around 15 Hz. Figures 3.9b and 3.9c display measurements for heated conditions. It can be seen in Figure 3.9b that under heated conditions, the base film thickness and the variance in film thickness have both decreased. The passage of waves can still be seen as spikes in the film thickness signal. The magnitude and frequency of the waves are significantly reduced. Cyclic dryout at critical heat flux is displayed in Figure 3.9c. For a position that is being rewet, the rate at which the film thickness suddenly increases is comparable to the rate at which disturbance waves pass. Furthermore, at CHF conditions the liquid film develops a quasiperiodic behavior. The quasiperiodic saw-toothed waves have a wave amplitude that is near the mean liquid-film

thickness, and vary in frequency between 3 and 5 Hz. This phenomenon was observed at similar vapor qualities for all mass fluxes investigated (for data containing other mass fluxes see Appendix B).

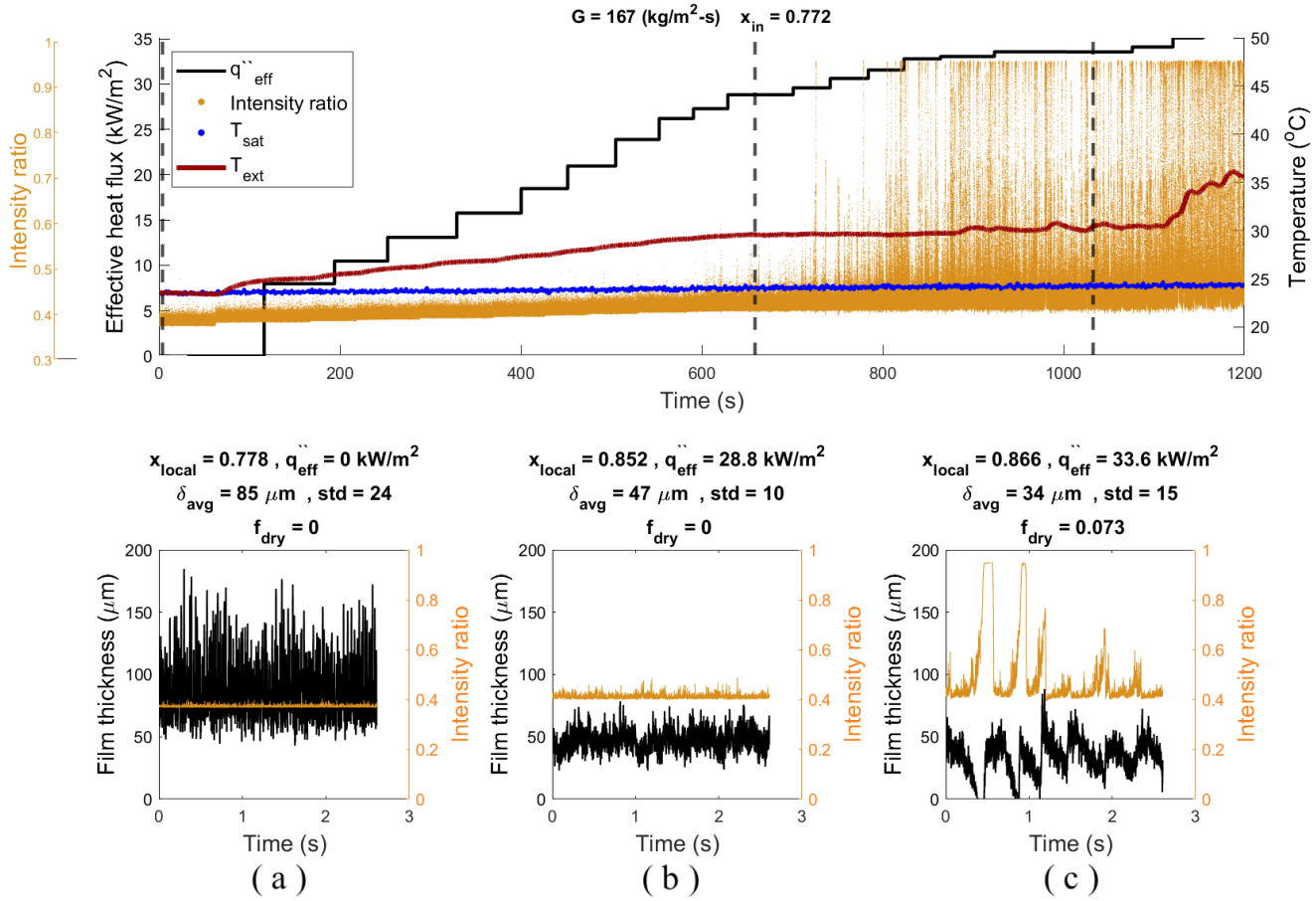

Figure 3.9: Time trace (top), film thickness and intensity ratio overlay (bottom). Dashed lines indicate the location of each film thickness measurement. A high CHF case for G = 167.4 kg/^{2}-s

3.5.2 Regime 2

In the second regime, x_{crit} has increased but CHF has decreased when compared to the previous regime. As with the previous case, 3.10a displays the measured film thickness for unheated conditions, and Figures 3.10b and 3.10c are for heated conditions. Prior to any dryout events, the behavior of the liquid film for unheated (Figure 3.10a) and heated (Figure 3.10b) conditions is similar to the previous regime. Figure 3.10c shows film thickness during

intermittent dryout and near CHF. The quasiperiodic behavior of the liquid film has been reduced but is still discernible. The amplitude and frequency of the apparent oscillations have both decreased compared to the oscillations observed in Figure 3.9c.

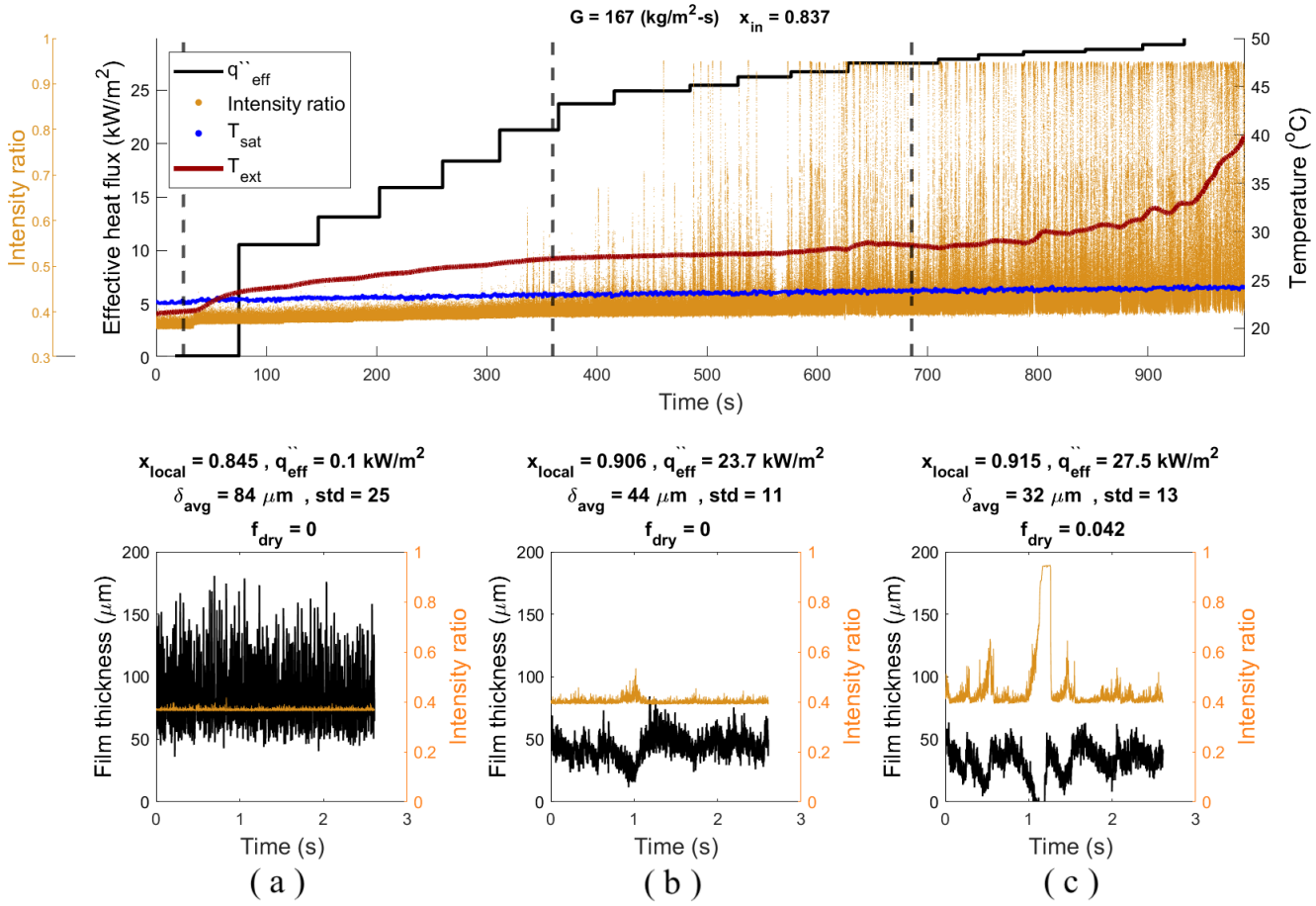

Figure 3.10: Time trace (top), film thickness and intensity ratio overlay (bottom). Middle range of heat flux and $G = 167.4$ kg/^{2}-s

3.5.3 Regime 3

The third and final regime lies on the far right-hand side of Figure 3.8. Film thickness measurements within this regime are captured in 3.11. The film-thickness signal for the unheated case, shown in Figure 3.11a, indicates that large disturbance waves are present for vapor qualities as high as $x_{local} = 0.90$. In Figure 3.11b, heating is applied and the liquid film thins. As heat flux increases the liquid film becomes thinner and gets very close to dryout

(Figure 3.11c), but the passing of a wetting front allows the film to return to a value close to the mean thickness. Figure 3.11d shows film thickness behavior for a heat flux higher than the CHF. Under these conditions the local liquid film is unstable and easily ruptures. The large wave like liquid structures observed in regime 1, appear to have completely vanished in regime 3.

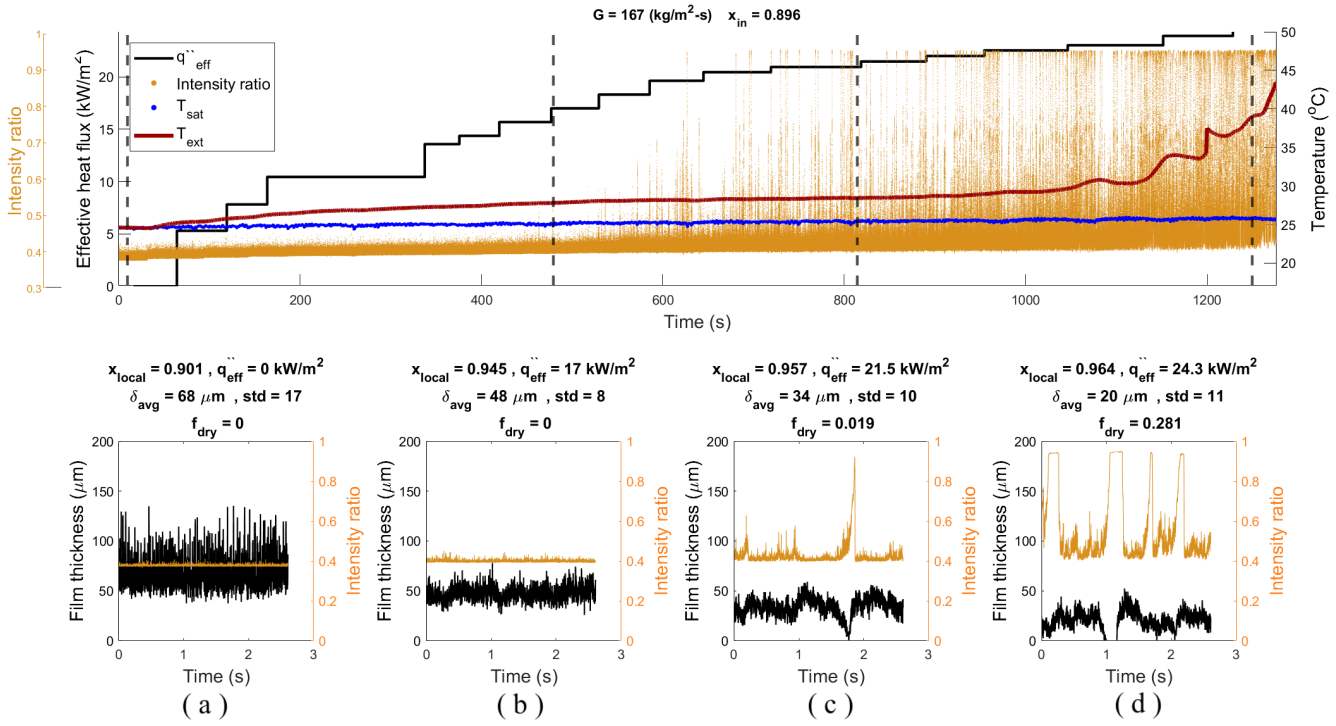

Figure 3.11: Time trace (top), film thickness and intensity ratio overlay (bottom). Dashed lines indicate the location of each film thickness measurement. A low CHF case for G = 167.4 kg/^{2}-s

3.6 Visualizing dryout

Liquid-film thickness data have shown the importance of waves in the cyclic dryout-rewetting process. In this section, high-speed videos provide further information about the behavior of the liquid film during dryout events. Figure 3.12 shows a sequence of images capturing a dryout event occurring in flow conditions similar to those in Figure 3.9. It can be seen that the liquid film begins to thin, resulting in the gradual disappearance of

surface features (ripples, etc.) occurring from t = 0 to 100 ms. The disappearance in surface features may be associated with the film thinning to a point where the viscous forces become dominant. The velocity of the surface features decreases during this stage and reaches near zero velocity at the time they are no longer visible. Once the surface features have completely vanished, the region will dry if more liquid is not supplied quickly (t = 150 - 200 ms). The red regions on Figure 3.12 indicate a dry region on the heated surface. The two dry regions that have formed quickly coalesce into a large dry region in the center of the channel (t = 200 ms). Another short period of time later, the surface is mostly dry with a column of liquid on the right hand side. An approaching wetting front can be seen as the blue line in Figure 3.12 (t = 250 ms).

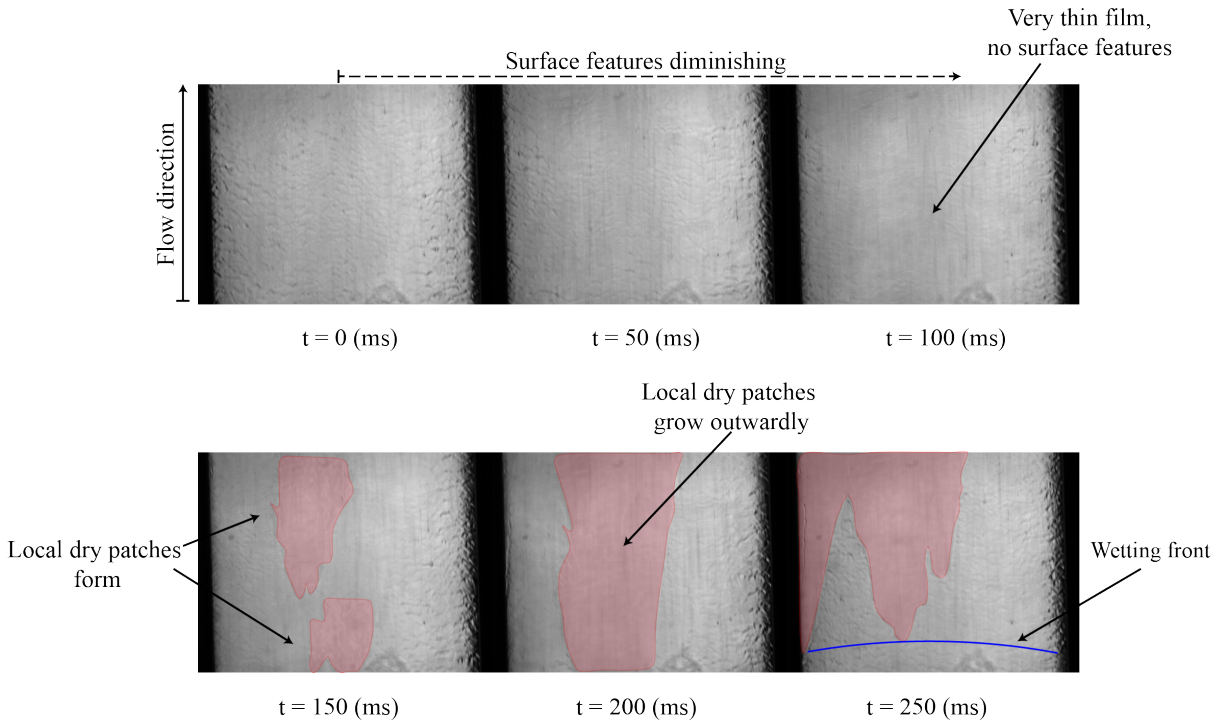

Figure 3.12: Annotated sequence of images capturing dryout with flow conditions $G = 167.5$ kg/m^2-s, $\dot{q}''_{eff} = 30.6$ kW/m^2, $X_{local} = .837$, $f_{dry} = 0.023$

Figure 3.13 displays a sequence of images that capture the rewet process immediately

following the dryout event shown in Figure 3.12. The dryout and rewet processes were observed to have different time scales; the rewetting of the surface occurs at a much faster rate. At the beginning of the rewet process, an initial wetting front composed of a thin film approaches the dry region (t = 275 - 280 ms). The initial front slows and eventually stalls at the position indicated by the solid blue line (t = 285 ms). Upstream from the location where the dry region and wetting front meet, a wave of thick film can be seen entering the frame and is indicated by the dashed blue line on Figure 3.13 (t = 290 ms). The thick-film wave catches up with the stalled wetting front, provides enough momentum to accelerate the front and eventually rewet the heated surface (t = 300 - 315 ms). The thick-film wave carrying a large mass of liquid in the stream-wise direction appears to be the remnant of a disturbance wave. An annotated video that captures the dryout-rewet sequence described in this section can be seen here: Dryout-rewet video [1]

[1] https://mediaspace.wisc.edu/media/Dryout-rewet/1_7sn93wd2

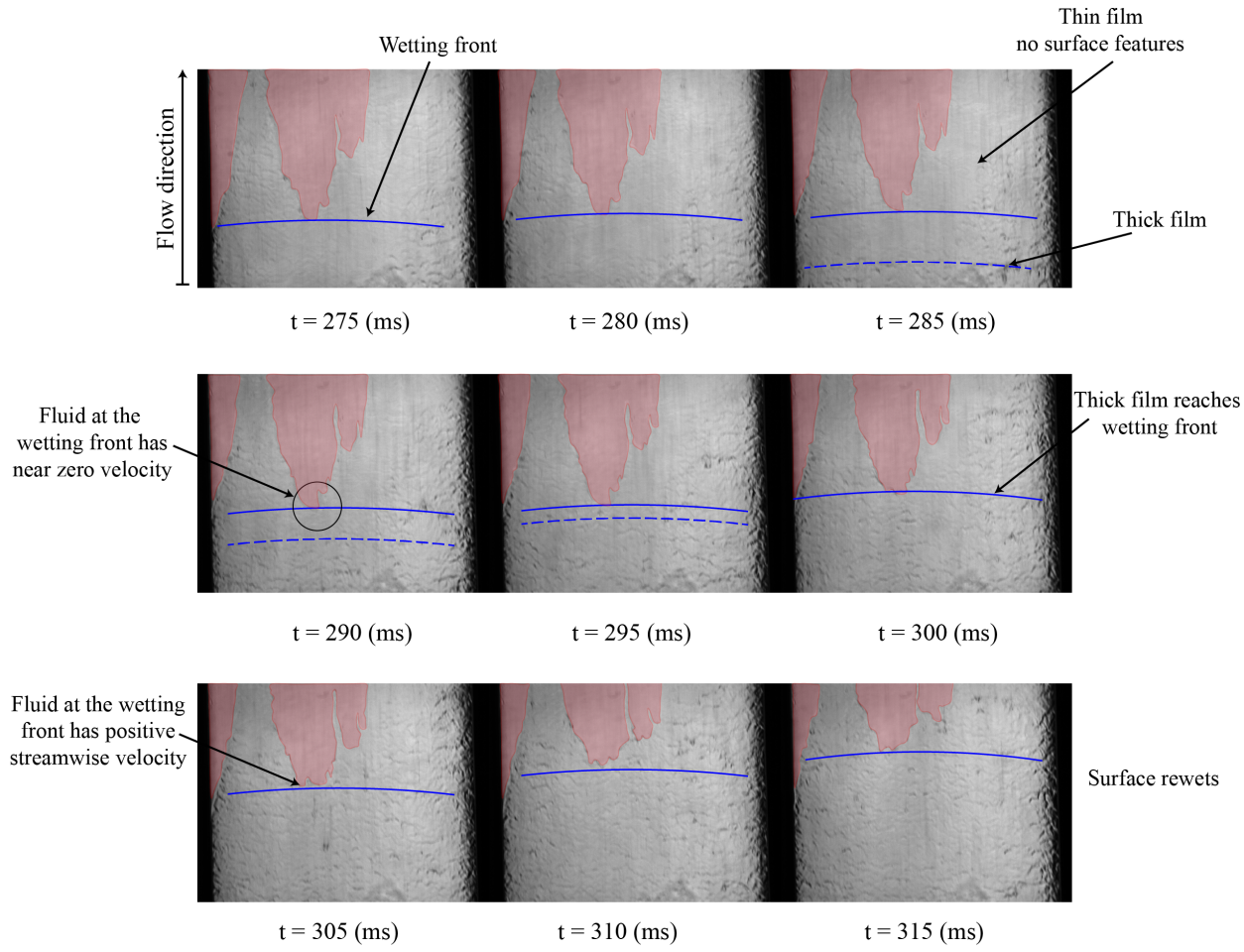

Figure 3.13: Annotated sequence of images capturing rewet immediately following dryout event shown in previous figure, with flow conditions $G = 167.5$ kg/m^2-s, $\dot{q}''_{eff} = 30.6$ kW/m^2, $x_{local} = .837$, $f_{dry} = 0.023$

3.7 Dryout statistics

Figure 3.14 shows the probability distribution of the duration of dryout events for various ranges of dry fractions. Similarly, Figure 3.15 shows the probability distribution of the time between dryout events for the same ranges of dry fractions. It is worth mentioning here that CHF was observed to occur at $f_{dry} \approx 0.05$. For low values of f_{dry}, there is greater occurrence of short dryout events and the spacing between the events is distributed nearly uniformly over a wide range of time values. For high values of f_{dry}, there is a wider distribution of the duration of any one dryout event and the time between events becomes less random and

quite short. For increasing f_{dry} there is a characteristic dryout time that occurs showing in the peak occurring in Figure 3.15 at approximately 0.25 seconds between dryout events. It was observed in the previous section through analysis of high-speed video that the dryout process takes longer time than the wetting process. If the wetting process is assumed to be nearly instantaneous then the time between dryout events is equal to the time it takes for a local position to dryout after a wetting front has passed that location.

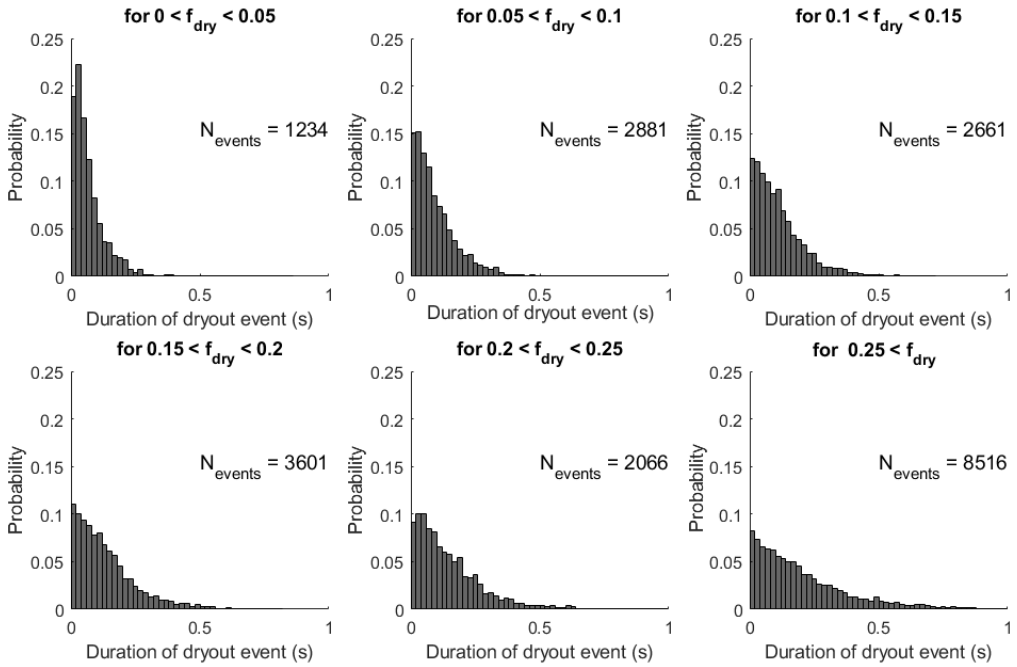

Figure 3.14: Probability distribution of the duration of dryout events for varying ranges of f_{dry}.

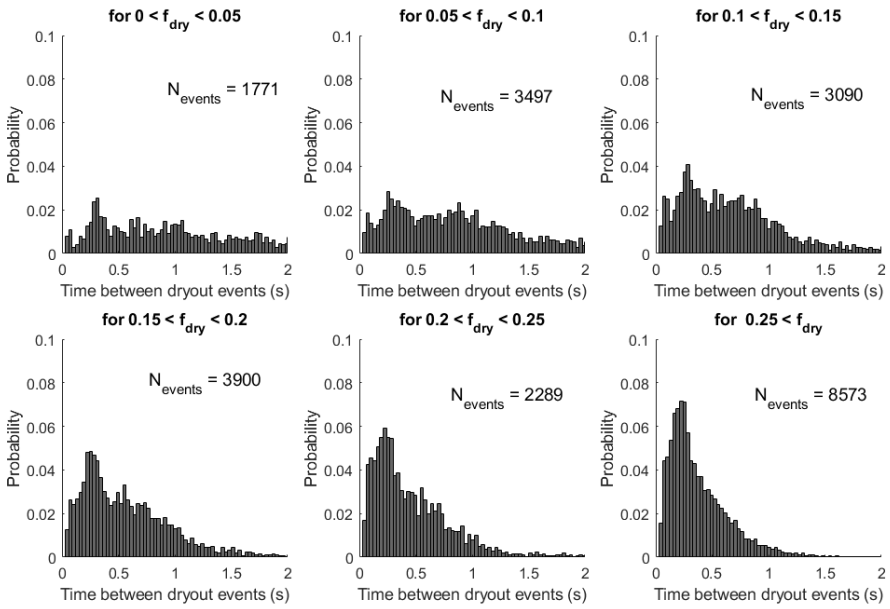

Figure 3.15: Probability distribution of the time between consecutive dryout events for varying ranges of f_{dry}.

Analysis of the high-speed videos shows that the bulk of the liquid transport is provided by the waves and that the rewetting process occurs on time scales that are much smaller than the drying process. It has also been observed that the velocity of the fluid in the wake of a wave is small relative to that of the disturbance wave itself. Furthermore, the measured film thickness during intermittent dryout was observed to be on the order of 30 to 40 μm and the thickness of the viscous sublayer is estimated to be on approximately 25 μm. Small perturbations at the interface could therefore expose the viscous sublayer at a local position to the vapor core. The increased contribution from viscous forces would dampen the propagation of surface ripples causing the liquid film to become smooth. As the liquid film becomes smoother there is less interfacial shear between vapor and liquid, further reducing the velocity of the liquid film. If the liquid film in the wake of a rewetting event were to become stationary, then time required to vaporize the film could be estimated as

$$t_{sfd} = \frac{\delta \rho_l \Delta i_{vap}}{\dot{q}''} \tag{3.3}$$

where δ is the liquid-film thickness and Δi_{vap} is the enthalpy of vaporization of R245fa.

For the conditions shown in Figure 3.9c, the viscous sublayer is to vaporize in approximately $t_{sfd} = 0.18$ seconds. For the conditions shown in Figure 3.10c, the estimated time it would take the film to vaporize is $t_{sfd} = 0.25$ seconds. Finally, for the conditions shown in subfigure of Figure 3.11d, it would take an estimated $t_{sfd} = 0.31$ seconds to vaporize the liquid film. The estimated time for dryout to occur after a rewetting event has occurred are in good agreement with the peak of the probability distributions shown in 3.15.

Data set	$\dot{q}''_{eff}$	t_{sfd}
Regime 1	33.6 kW/m^2	0.18 s
Regime 2	27.5 kW/m^2	0.25 s
Regime 3	24.3 kW/m^2	0.31 s

Table 3.2: Estimated dryout times for varying flow conditions

For flows with increasing dry fractions, this behavior is observed more clearly. Figure 3.16 displays images capturing consecutive dryout events. The thick-film wave wets the surface and leaves behind a film that is nearly as thin as the viscous sublayer and possesses small streamwise velocity. The film in the wake of the wave dries out approximately $t_{sfd} = 0.25$ seconds after the wave passes.

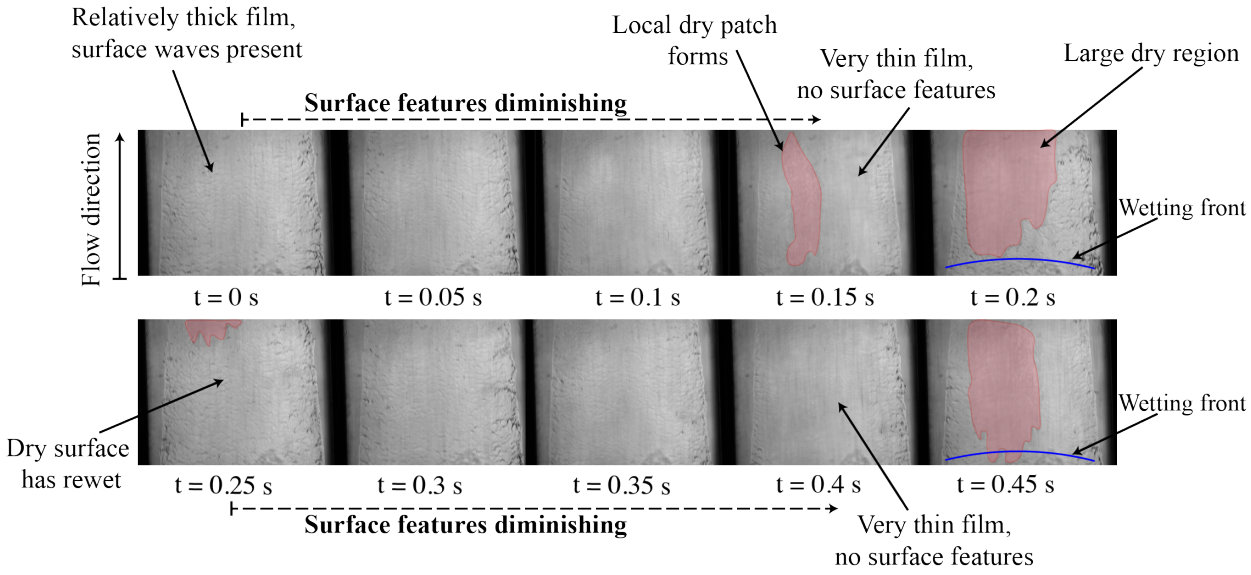

Figure 3.16: Annotated sequence of images capturing sequential dryout events $G = 167.5$ kg/m^2-s, $\dot{q}''_{eff} = 34.8$ kW/m^2, $x_{local} = .867$, $f_{dry} = 0.211$

Chapter 4

Conclusion

Dryout of liquid film and CHF in annular flow through a vertical rectangular channel has been characterized. A temporal dry fraction, f_{dry}, is measured using an optical technique derived from Fehring et al. (2020) and is related to the measured HTC. The liquid-film thickness is measured using an optical technique introduced by Hurlburt and Newell (1996), and refined by Moreira et al. (2020). Based on the experimental results, the following conclusions are made:

- A quantitative description of the CHF in flow boiling at high vapor qualities has been provided. For a local position and specified flow conditions, CHF is the value of heat flux when a local maximum in HTC occurs. Any increase in heat flux past the CHF will result in reducing the HTC and increasing the surface temperature.

- The dryout of liquid film occurs prior to a reduction in HTC and therefore prior to the heat flux reaching the level of CHF. The heat flux associated with the first occurrence of dryout events, DHF, was found to be on average 90% of the CHF value. However, in extremely high vapor quality conditions the value of DHF was as low as 50% of the CHF.

- A normalized HTC, $\mathcal{H}$, is calculated based on the two-phase HTC prior to dryout, h_{tp}, and the HTC of the single-phase vapor, h_v. For $0 < f_{dry} < 0.05$, the value of

$\mathcal{H}$ increases between 10-25%. For all mass fluxes investigated in this study, the CHF occurs when the local position has a dry fraction of $f_{dry} \approx 0.05$.

- The behavior of the liquid film during the heated and cyclic dryout conditions is characterized and broken into three regimes of increasing vapor quality. In the first regime, the fluid possesses relatively low vapor quality and therefore more fluid in the liquid phase. The liquid film develops quasiperiodic saw-tooth wave structures during cyclic dryout conditions near CHF. In regime 2, vapor quality is increased and the quasiperiodic behavior of the waves is reduced, though still observed. Further increasing vapor quality into regime 3, the liquid film no longer exhibits the quasi-periodic waves. The decrease in CHF between regimes 1, 2, and 3 may be related to the liquid's ability to form the wave structures.

- The dryout mechanism is observed. For dryout to occur at a local position, the liquid film first becomes very smooth and the liquid film may rupture. Once formed, the dry regions grow fast in the streamwise direction. Dry regions that form close to one another quickly coalesce into a large dry region.

- The rewetting mechanism is also observed. The rewetting process was found to occur at a much faster rate than the drying process and is governed by the passage of waves in the liquid film. Especially for high heat fluxes, the initial wetting front is observed to stall when the rate at which liquid is supplied to a local region is equal the rate at which it vaporizes. The passage of a thick-film wave accelerates the wetting front and allows for the heated surface to be rewet.

- The temporal dry fraction, f_{dry}, indicates the fraction of time that the local position within the test section is dry. Statistics pertaining to duration of dryout events and the time between dryout events are presented for thousands of dryout events. For increasing f_{dry}, there is a characteristic time between dryout events (wet duration) of 0.25 s.

- For cyclic dryout events, the liquid-film thickness in the wake of a wetting event is observed to be on the order of the viscous sublayer. In addition, the fluid in the wake is observed to have small streamwise velocity relative the wave. By approximating the fluid left in the wake of a wetting event as stationary, a dryout time, t_{sfd}, is calculated. The estimates provided from the stationary film assumption agree with the characteristic dryout time observed in the PDFs. In addition, high-speed video capturing consecutive dryout events is used to confirm this observation.

To the author's knowledge, no other study in the literature has provided such a complete analysis of the dryout mechanism, the CHF, and the transition to boiling crisis. However, this study only includes analysis for a single fluid and a small range of mass fluxes. Further studies of this nature need to be performed for a wider range of mass fluxes and different types of fluids.

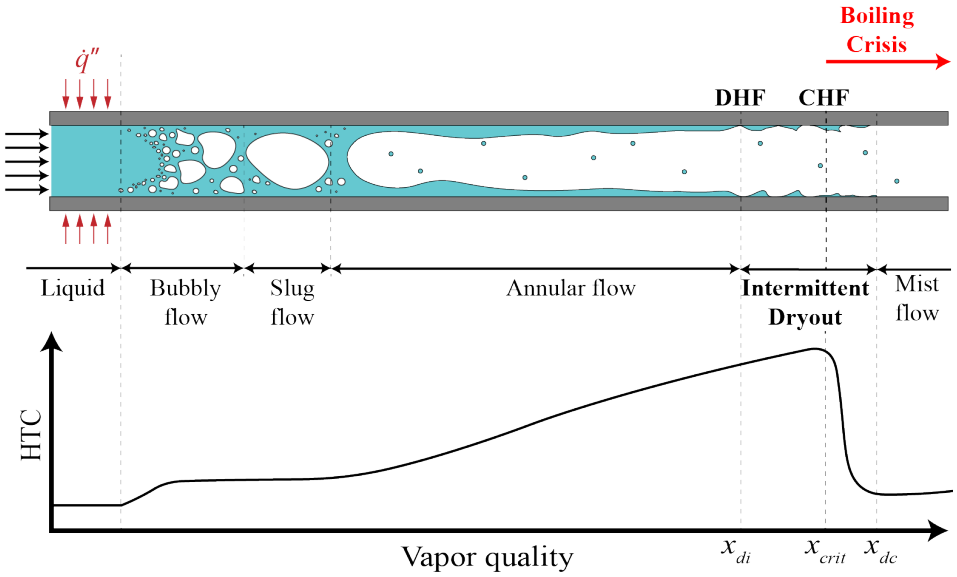

Figure 4.1: Updated flow boiling regimes figure, including the intermittent dryout regime

An updated version of our regime progression is shown in Figure 4.1. The new figure includes the maximum heat transfer coefficient and CHF occurring within the intermittent dryout regime. Many applications in industry consciously decide to operate in conditions

far from the dryout as a measure of caution. However, heat transfer coefficient is maximized in a regime of intermittent dryout. By operating far from this region, additional cooling capacity is being wasted. Therefore, the underlying physics that govern the dryout and rewet mechanisms need further investigation in order to utilize the increased heat transfer in flows with controlled dryout.

Bibliography

Abernethy, R. and Thompson, J. (1973). Handbook of uncertainty in gas turbine measurements. *Nat. Tech. Inform. Serv.*

Ahn, H., Lee, C., Kim, H., Jo, H., Kang, S., Kim, J., Shin, J., and Kim, M. H. (2010). Pool boiling CHF enhancement by micro/nanoscale modifications of zircaloy-4 surface. *Nuclear Engineering and Design*, 240(10):3350–3360.

Anwar, Z., Palm, B. E., and Khodabandeh, R. (2015). Dryout characteristics of natural and synthetic refrigerants in single vertical mini-channels. *Experimental Thermal and Fluid Science*, 68:257–267.

Blasius, P. R. H. (1913). Das aehnlichkeitsgesetz bei reibungsvorgangen in flussigkeiten. *Forschungsheft*, 131:1–141.

Borhani, N., Agostini, B., and Thome, J. R. (2010). A novel time strip flow visualisation technique for investigation of intermittent dewetting and dryout in elongated bubble flow in a microchannel evaporator. *International Journal of Heat and Mass Transfer*, 53:4809–4818.

Borhani, N. and Thome, J. R. (2014). Intermittent dewetting and dryout of annular flows. *International Journal of Multiphase Flow*, 67:144–152.

Colebrook, C. (1939). Turbulent flow in pipes, with particular reference to the transition

between the smooth and rough pipe laws. *Journal of the Institution of Civil Engineers*, 11(4):133–156.

Collier, J. and Thome, J. R. (1994). Convective boiling and condensation. *3rd ed. Oxford: Clarendo Press*.

Del Col, D. and Bortolin, S. (2012). Investigation of dryout during flow boiling in a single microchannel under non-uniform axial heat flux. *International Journal of Thermal Sciences*, 57:12–36.

Del Col, D., Fantini, F., and Rossetto, L. (2007). Dryout quality in a minichannel flow boiling. *XXV UIT National Heat Transfer Conf., Italy*, pages 18–20.

Diani, A., Mancin, S., Balcon, M., Savio, E., and Rossetto, L. (2018). R1234yf flow boiling heat transfer in a rectangular channel heated from the bottom. *Heat Transfer Engineering*, 39(3):198–207.

Dittus, F. and Boelter, L. (1930). Heat transfer in automobile radiators of the tubular type. *Publications in Engineering*, 2:443–461.

Fehring, B., Morse, R., Chan, J., Dressler, K., Hurlburt, E., Nellis, G., and Berson, A. (2020). Instantaneous optical measurement of the temperature at the interface between a wall and a thin liquid film. *Journal of Heat Transfer*, 142(121701).

Galloway, J. and Mudawar, I. (1993). Chf mechanism in flow boiling from a short heated wall - I: Examination of near-wall conditions with the aid of photomicrography and high-speed video imaging. *International Journal of Heat and Mass Transfer*, 36(10):2511–2526.

Gnielinski, V. (1975). *Forsch Ing-Wes*, 41.

Groeneveld, D. (2012). The 2006 chf look-up table. *Nuclear Engineering and Design*, 237:1909–1922.

Hurlburt, E. and Newell, T. (1996). Optical measurement of liquid film thickness and wave velocity in liquid film flows. *Experiments in Fluids*, 21:357–362.

Jabardo, J. and Bandarra-Filho, E. (2000). Convective boiling of halocarbon refrigerants flowing in a horizontal copper tube - an experimental study. *Experimental Thermal and Fluid Science*, 23:93–104.

Kanizawa, F. T., Tibiriçá, C. B., and Ribatski, G. (2016). Heat transfer during convective boiling inside microchannels. *International Journal of Heat and Mass Transfer*, 93:566–583.

Katto, Y. and Ohno, H. (1984). An improved version of the generalized correlation of critical heat flux for the forced convective boiling in uniformly heated vertical tubes. *International Journal of Heat and Mass Transfer*, 27:1641–1648.

Kim, S. and Mudawar, I. (2013). Universal approach to predicting saturated flow boiling heat transfer in mini/micro-channels (Part I) dryout incipience quality. *International Journal of Heat and Mass Transfer*, 64:1226–1238.

Klein, S. (2019). Engineering equation solver (EES). Academic.

Lillo, G., Mastrullo, R., Mauro, A., and Viscito, L. (2019). Flow boiling of R1233zd(e) in a horizontal tube: Experiments, assessment and correlation for asymmetric annular flow. *International Journal of Heat and Mass Transfer*, 129:547–561.

Mancin, S., Diani, A., and Rossetto, L. (2016). Flow boiling heat transfer, dewetting-rewetting, and dryout visualization of hfos in an asymmetrically heated rectangular plain channel. *Applied Thermal Engineering*, 107:960–974.

Marathe, S. and Webb, R. L. (2008). Prediction of dryout vapor quality for annular two-phase flow in tubes. *Applied Thermal Engineering*, 28:691–698.

Mastrullo, R., Mauro, A., Thome, J., Toto, D., and Vanoli, G. (2012). Flow pattern maps for convective boiling of CO_2 and R410A in a horizontal smooth tube: Experiments and new correlations analyzing the effect of the reduced pressure. *International Journal of Heat and Mass transfer*, 55:1519 – 1528.

Moreira, T. A., Morse, R. W., Dressler, K. M., Ribatski, G., and Berson, A. (2020). Liquid-film thickness and disturbance-wave characterization in a vertical, upward, two-phase annular flow of saturated R245fa inside a rectangular channel. *International Journal of Multiphase Flow*, 132(103412).

Mori, H., Yoshida, S., Ohishi, K., and Kokimoto, Y. (2000). Dryout quality and post dryout heat transfer coefficient in horizontal evaporator tubes. *Proc of 3rd European Thermal Sciences Conference*, pages 839–844.

Nascimento, F. J., Moreira, T. A., and Ribatski, G. (2019). Flow boiling critical heat flux of DI-water and nanofluids inside smooth and nanoporous round microchannels. *International Journal of Heat and Mass Transfer*, 139:240–253.

National Instruments (2019). Software. LabView.

Nellis, G. and Klein, S. (2009). *Heat Transfer*. Cambridge University Press.

Ong, C. and Thome, J. (2011). Macro-to-microchannel transition in two-phase flow: Part 2 flow boiling heat transfer and critical heat flux. *Experimental Thermal and Fluid Science*, 35:873–886.

Petukhov, B. (1970). Heat transfer and friction in turbulent pipe flow with variable physical properties. *Advances in heat transfer*, 6c:503–564.

Qu, W. and Mudawar, I. (2002). Prediction and measurement of incipient boiling heat flux in micro-channel heat sinks. *International Journal of Heat and Mass Transfer*, 45:3933–3945.

Revellin, R., Haberschill, P., Bonjour, J., and Thome, J. R. (2008). Conditions of liquid film dryout during saturated flow boiling in microchannels. *Chemical Engineering Science*, 63:5795–5801.

Shah, M. M. (1987). Improved general correlation for critical heat flux during upflow in uniformly heated vertical tubes. *International Journal of Heat and Fluid Flow*, 8(4):326–335.

Shedd, T. and Newell, T. (1998). Automated optical liquid film thickness measurement method. *The American Institute of Physics - Review of Scientific Instruments*, 69.

Taylor, B. and Kuyatt, C. (1994). Guidelines for evaluating and expressing the uncertainty of NIST measurement results. *NIST Technical note 1927: Edinton, Gaithersburg, 1994*.

Tibiriçá, C. B., Ribatski, G., and Thome, J. R. (2012). Saturated flow boiling heat transfer and critical heat flux in small horizontal flattened tubes. *International Journal of Heat and Mass Transfer*, 55(25-26):7873–7883.

Wojtan, L., Revellin, R., and Thome, J. R. (2006). Investigation of saturated critical heat flux in a single uniformly heated microchannel. *Experimental Thermal and Fluid Science*, 20:765–774.

Wojtan, L., Ursenbacher, T., and Thome, J. R. (2005). Investigation of flow boiling in horizontal tubes: Part 1 a new diabatic two-phase flow pattern map. *International Journal of Heat and Mass Transfer*, 48:2955–2969.

Zhang, B., Kim, K., and Yoon, H. (2012). Enhanced heat transfer performance of alumina sponge-like nano-porous structures through surface wettability control in nucleate pool boiling. *International Journal of Heat and Mass Transfer*, 55(25-26):7487–7498.

Zhang, W., Hibiki, T., Mishima, K., and Mi, Y. (2006). Correlation of critical heat flux for

flow boiling of water in mini-channels. *International Journal of Heat and Mass Transfer*, 49(5-6):1058–1072.

Zhao, T., Markides, C. N., Matar, O. K., and Hewitt, G. F. (2013). Disturbance wave development in two-phase gas–liquid upwards vertical annular flow. *nternational Journal of Multiphase Flow*, 55:111–129.

Appendix A

Time series of flow conditions

A.1 Mass flux $G = 130$ kg/m^2-s

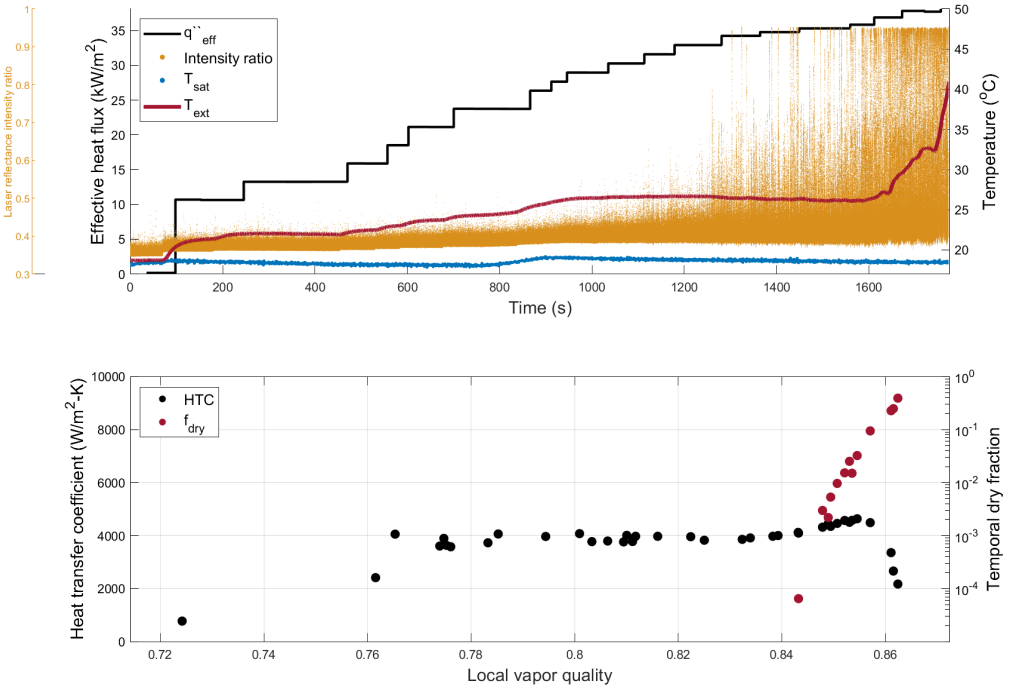

Figure A.1: $G = 128$ kg-m^2-s , $x_{in} = 0.72$

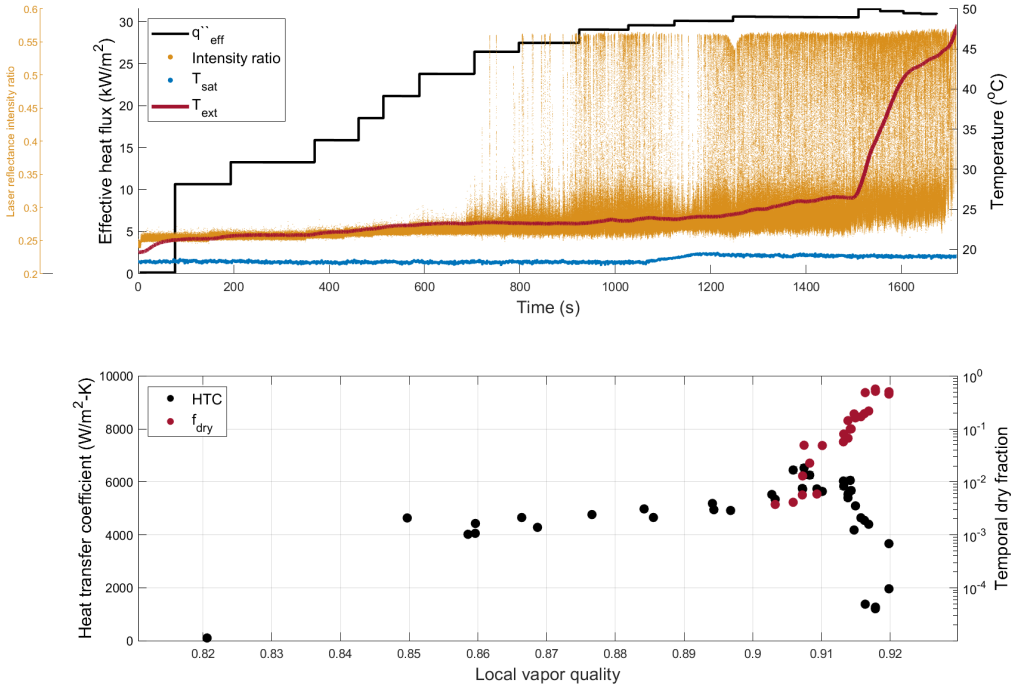

Figure A.2: $G = 128$ kg-m^2-s , $x_{in} = 0.81$

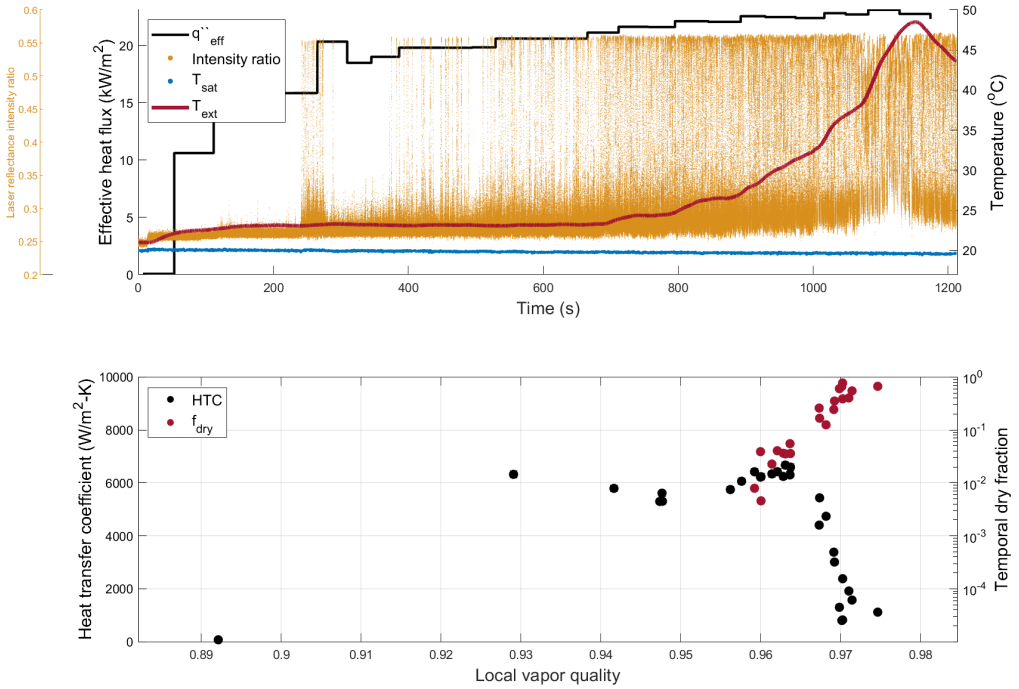

Figure A.3: $G = 128$ kg-m^2-s , $x_{in} = 0.89$

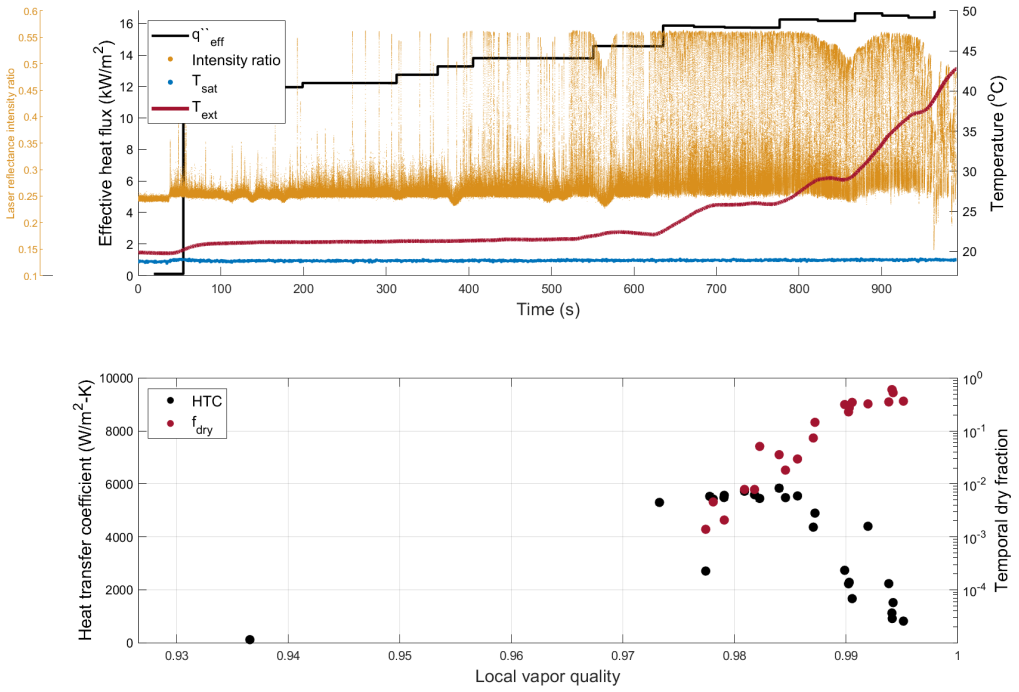

Figure A.4: $G = 128$ kg-m^2-s , $x_{in} = 0.93$

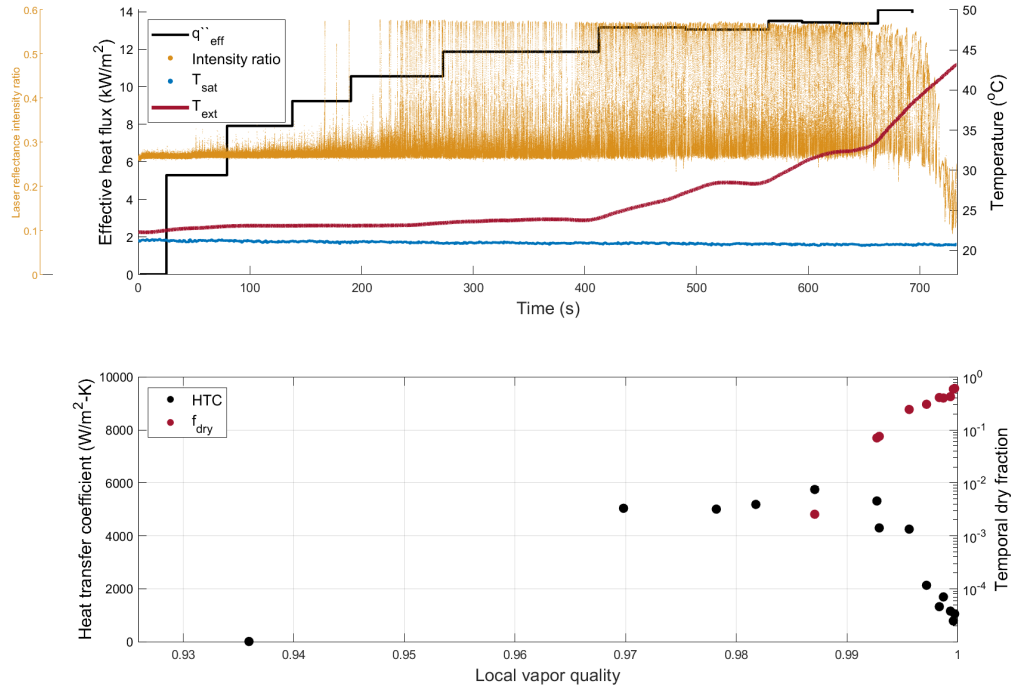

Figure A.5: $G = 130$ kg-m^2-s , $x_{in} = 0.95$

A.2 Mass flux $G = 140$ kg/m^2-s

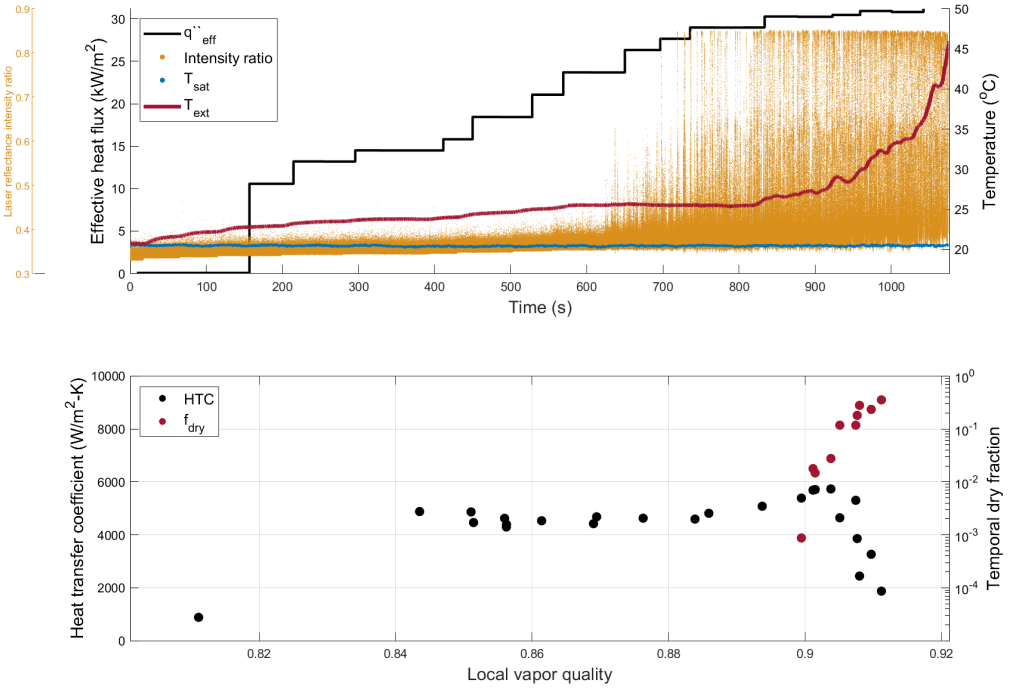

Figure A.6: $G = 140$ kg-m^2-s , $x_{in} = 0.81$

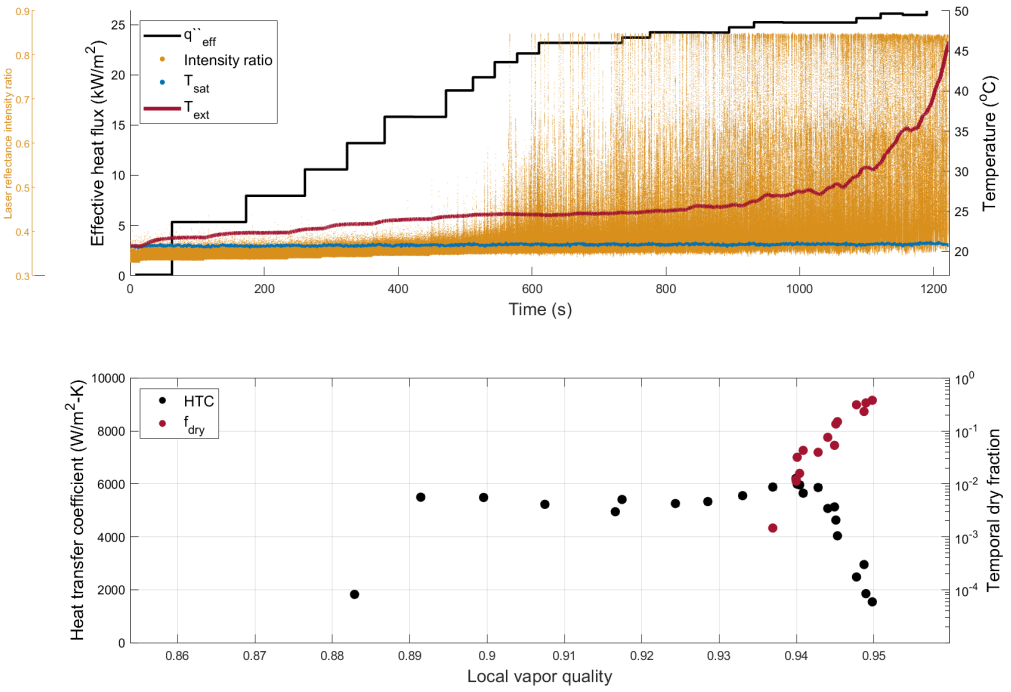

Figure A.7: $G = 140$ kg-m^2-s , $x_{in} = 0.86$

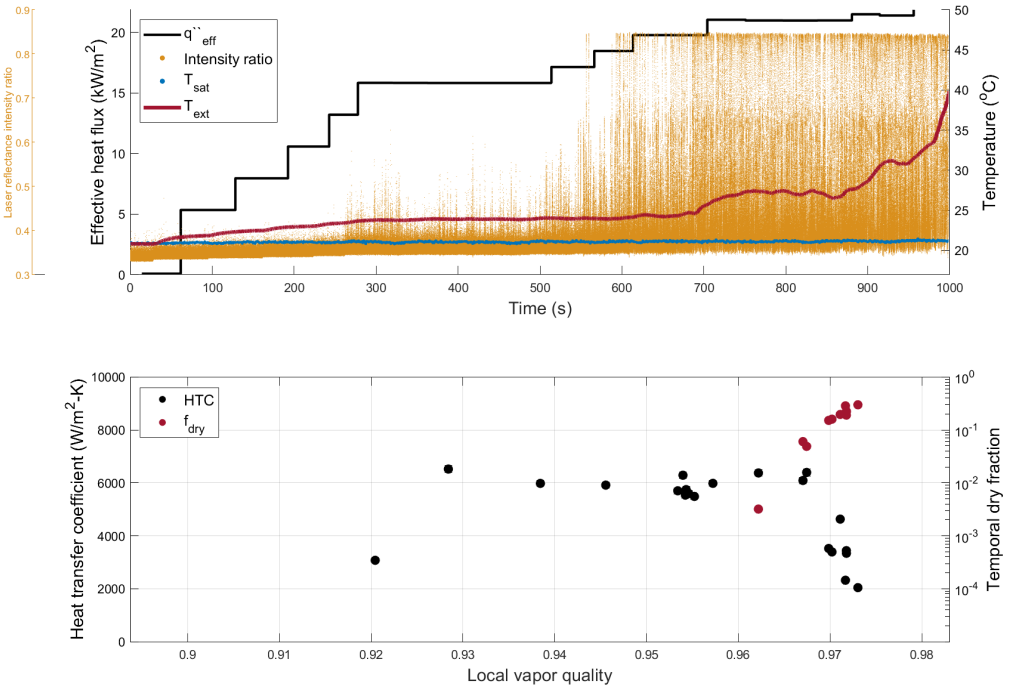

Figure A.8: $G = 140$ kg-m^2-s , $x_{in} = 0.90$

A.3 Mass flux $G = 150$ kg/m^2-s

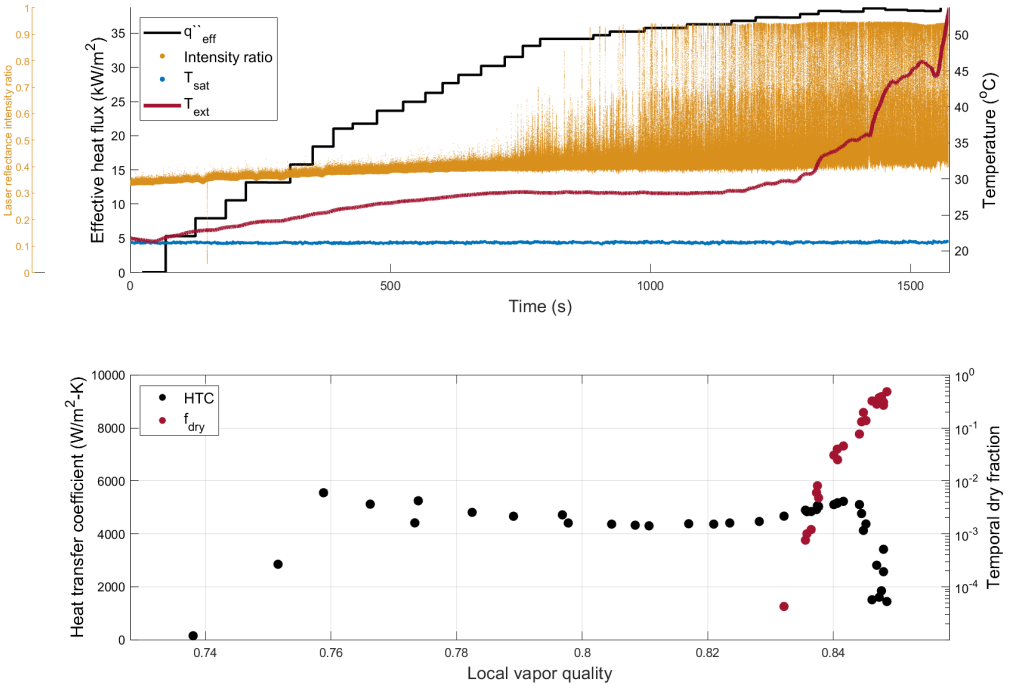

Figure A.9: $G = 149$ kg-m^2-s , $x_{in} = 0.73$

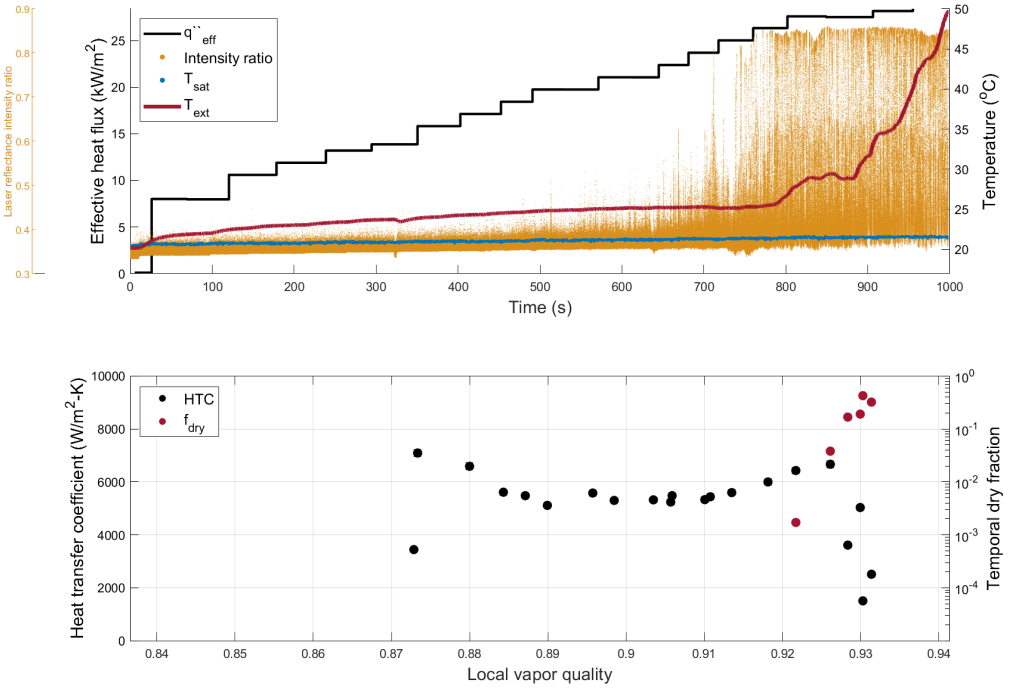

Figure A.10: $G = 149$ kg-m^2-s , $x_{in} = 0.84$

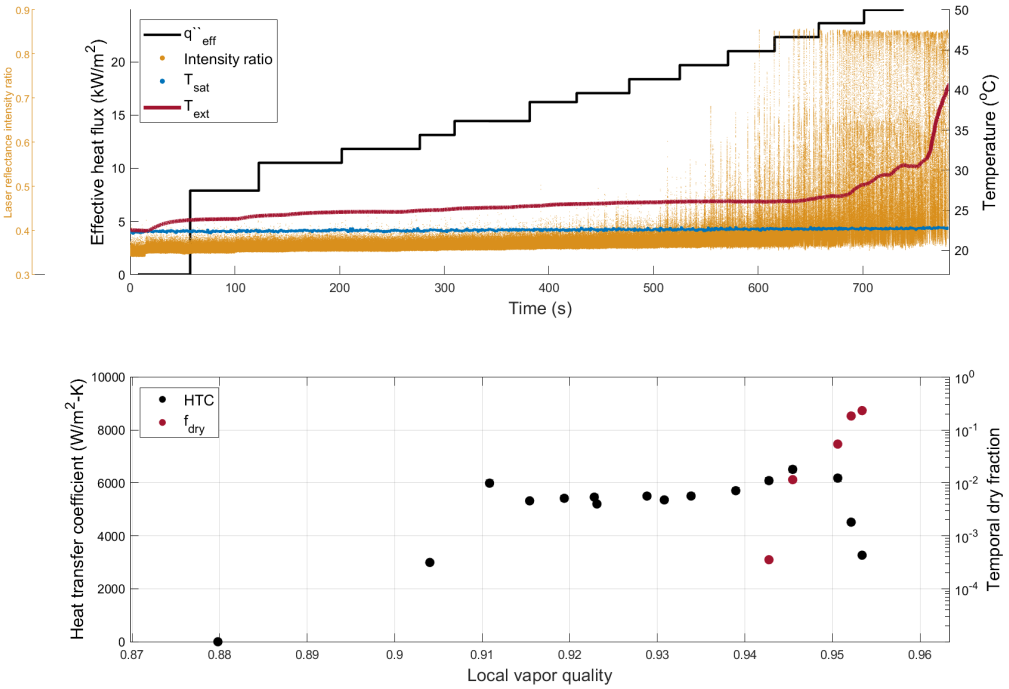

Figure A.11: $G = 149$ kg-m^2-s , $x_{in} = 0.88$

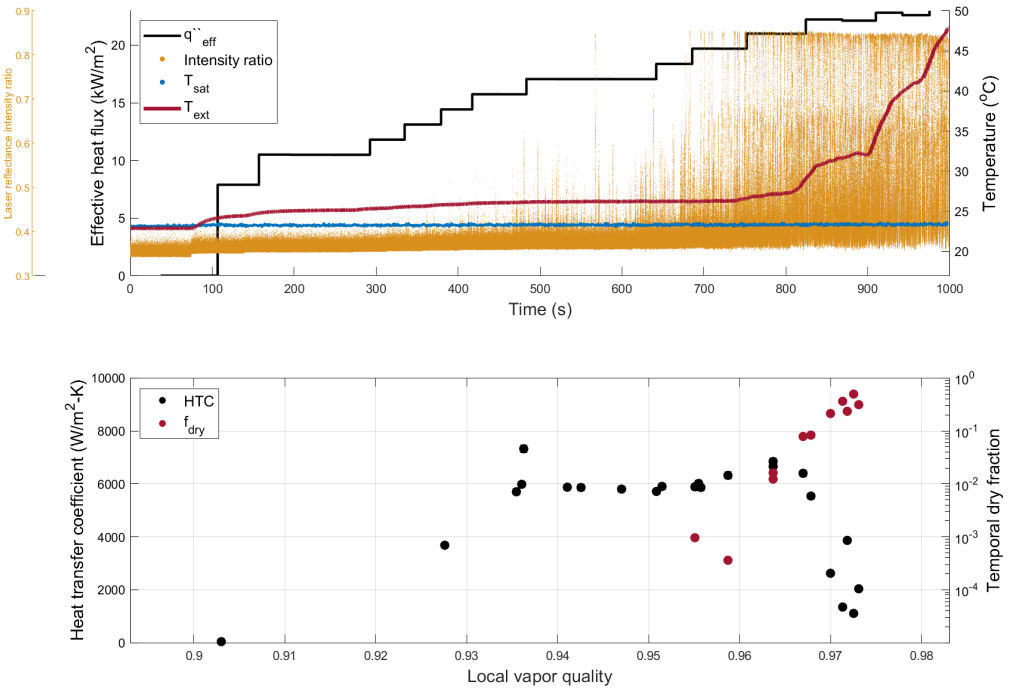

Figure A.12: $G = 149$ kg-m^2-s , $x_{in} = 0.90$

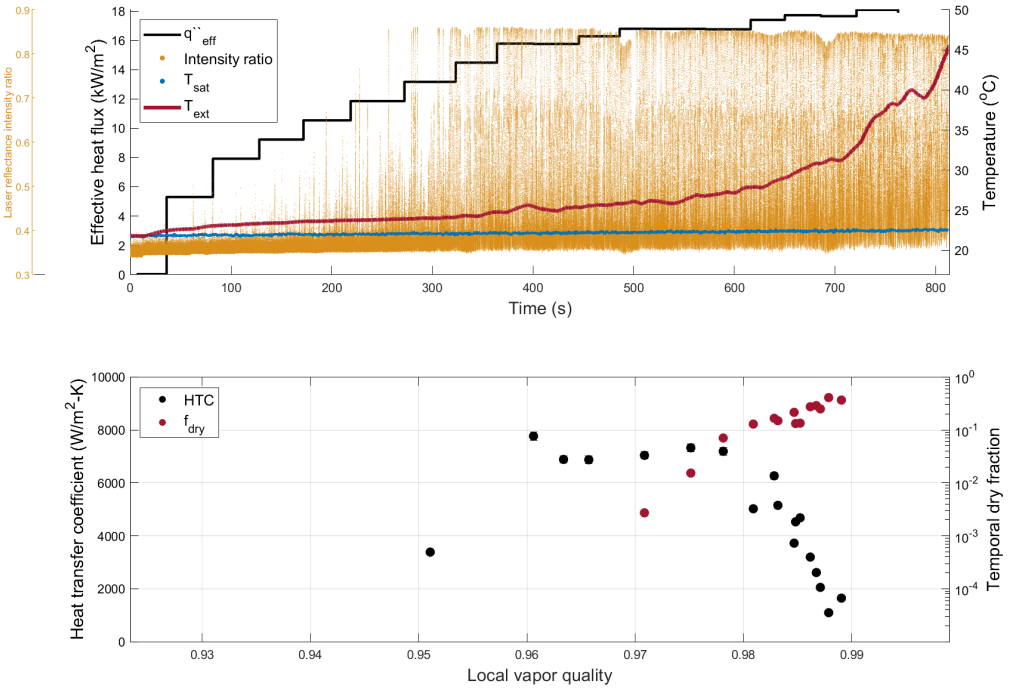

Figure A.13: $G = 149$ kg-m^2-s , $x_{in} = 0.93$

A.4 Mass flux $G = 167$ kg/m^2-s

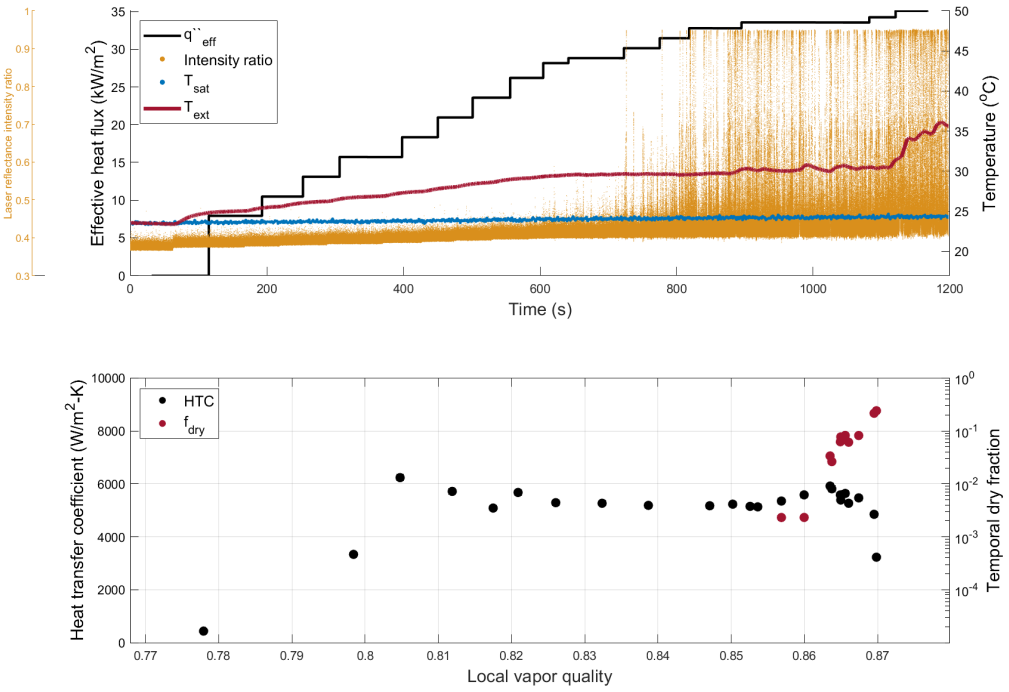

Figure A.14: $G = 167$ kg-m^2-s , $x_{in} = 0.77$

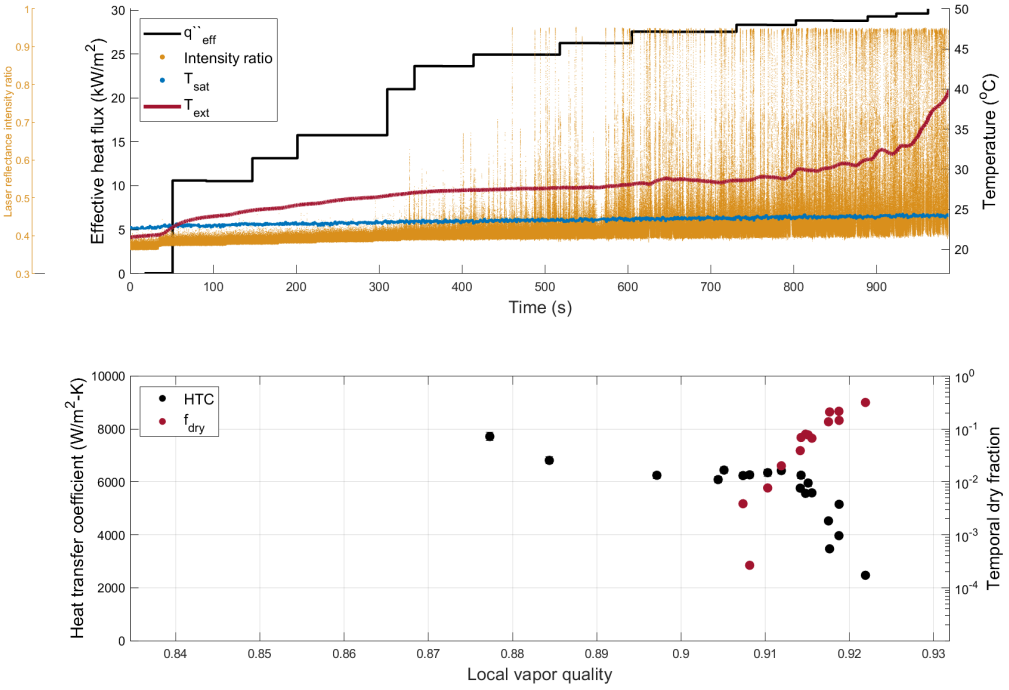

Figure A.15: $G = 167$ kg-m^2-s , $x_{in} = 0.84$

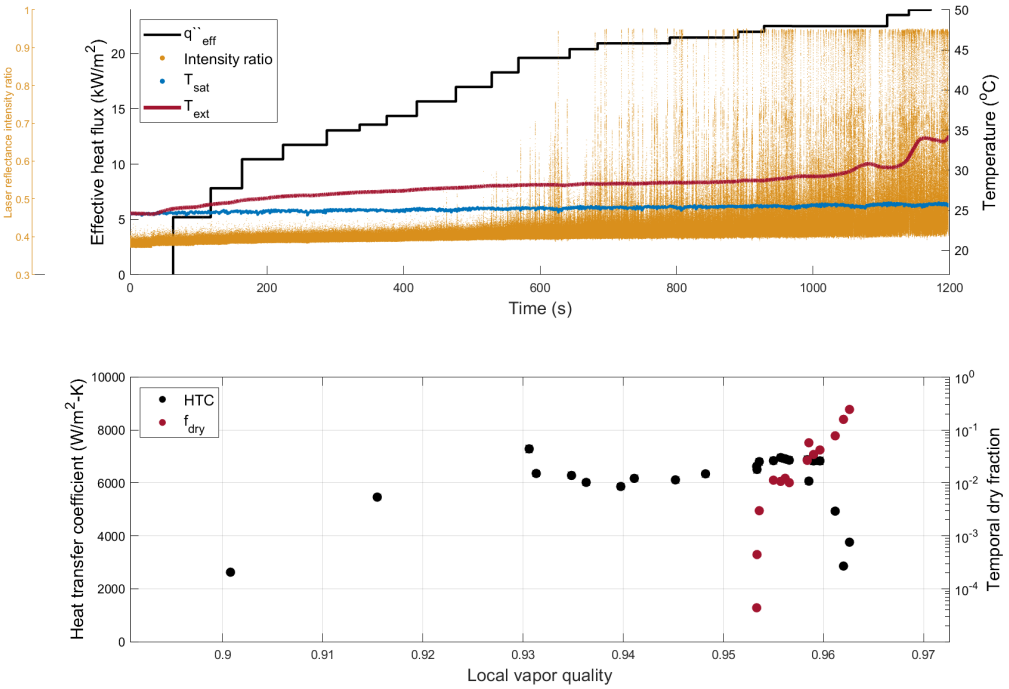

Figure A.16: $G = 167$ kg-m^2-s , $x_{in} = 0.90$

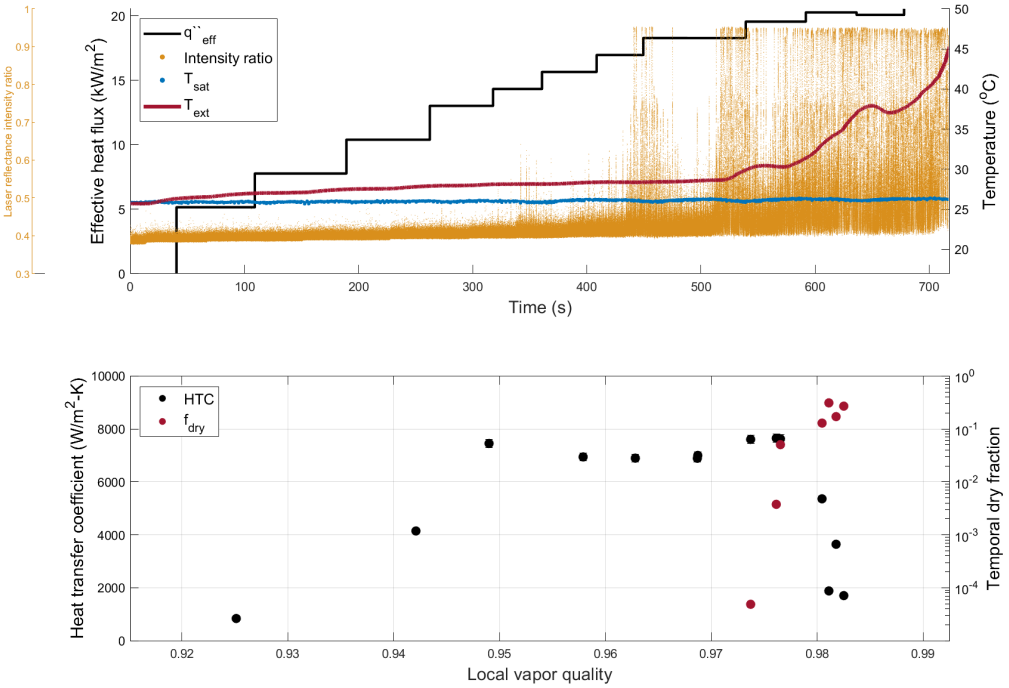

Figure A.17: $G = 167$ kg-m^2-s , $x_{in} = 0.92$

Appendix B

Film thickness

B.1 Mass flux $G = 130$ kg/m^2-s

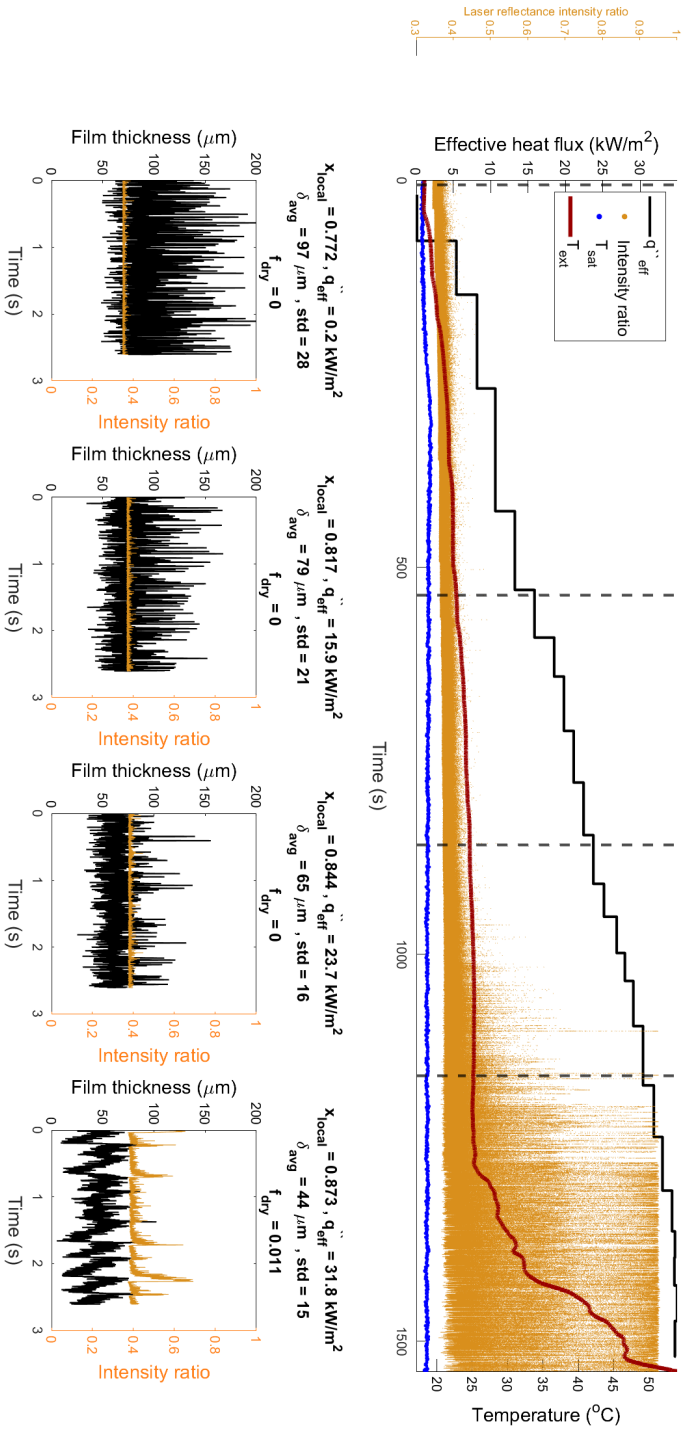

Figure B.1: $G = 129$ kg-m^2-s , $x_{in} = 0.772$

B.2 Mass flux $G = 150$ kg/m^2-s

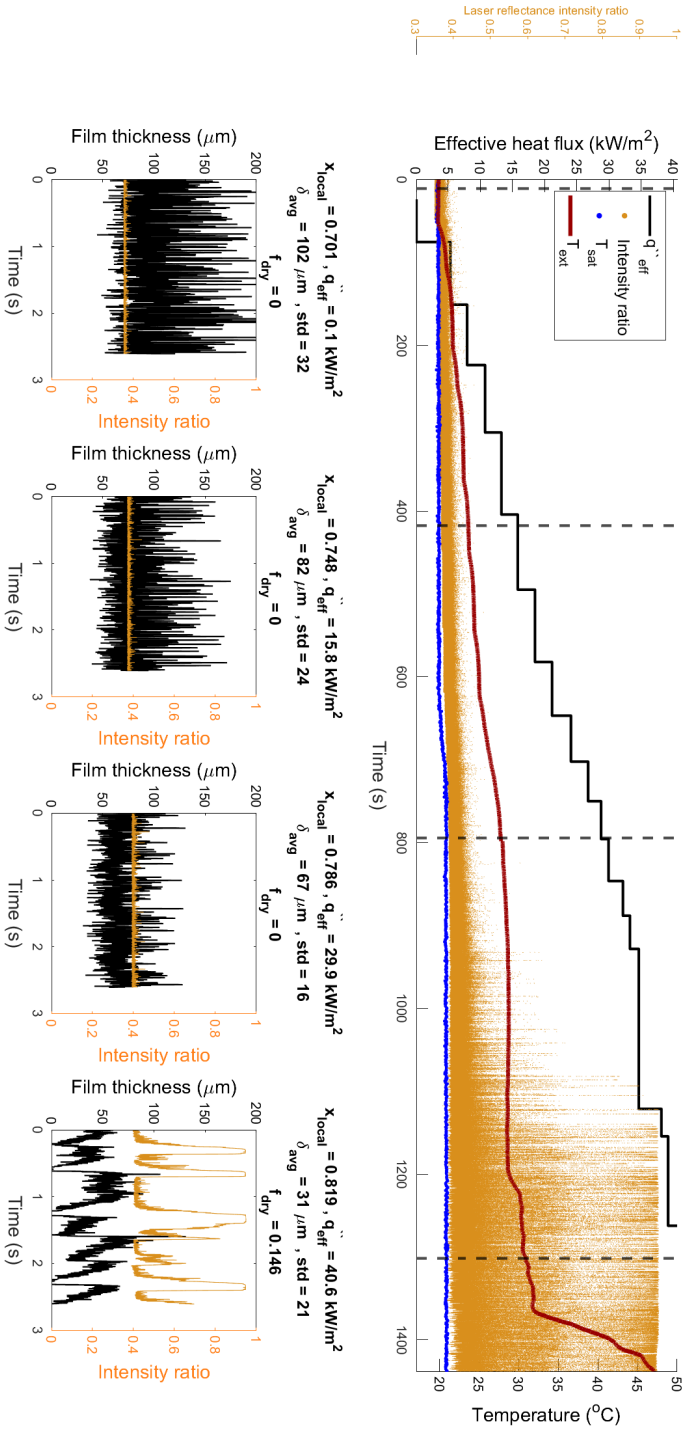

Figure B.2: $G = 149$ kg-m^2-s , $x_{in} = 0.694$

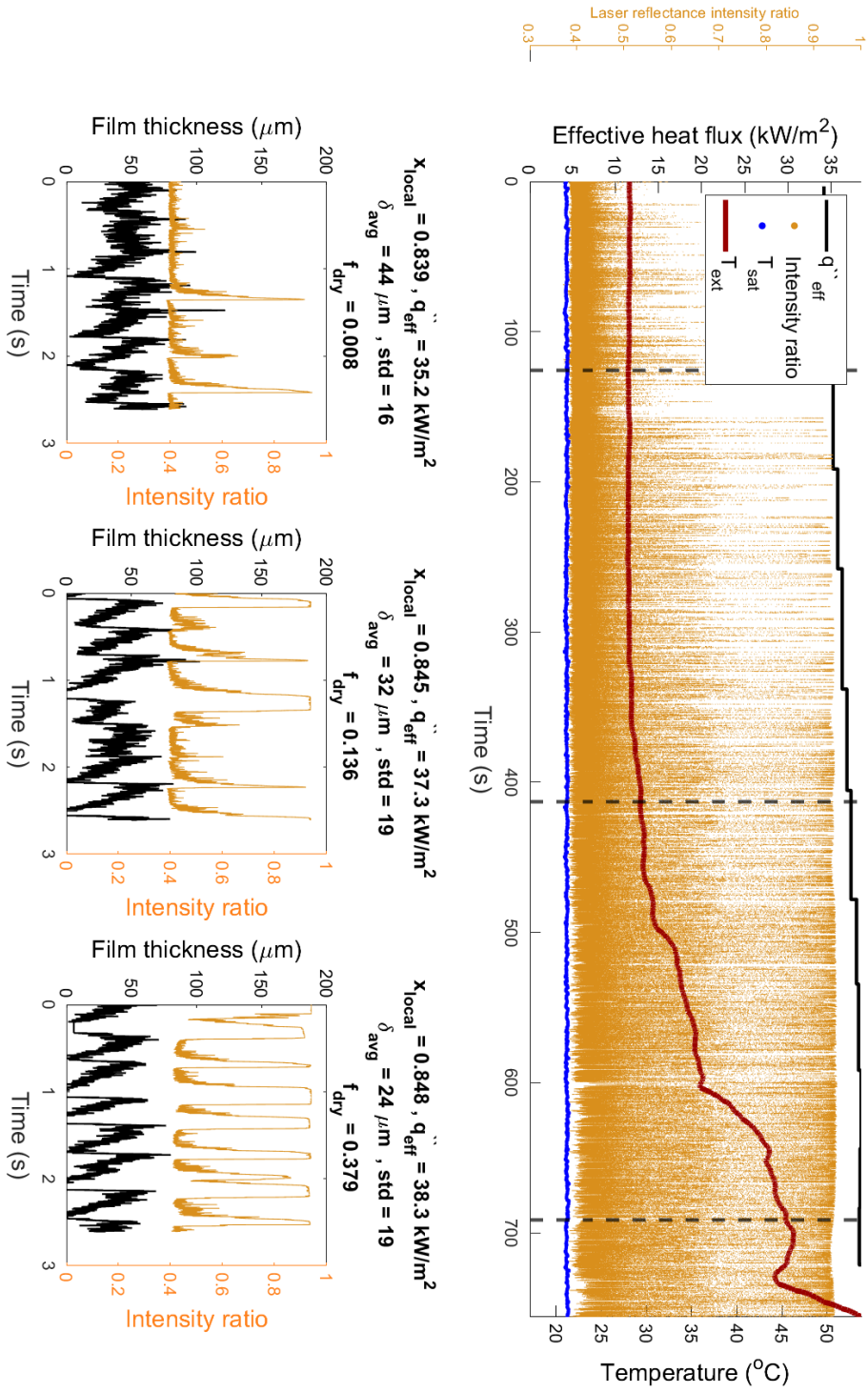

Figure B.3: $G = 149$ kg-m^2-s , $x_{in} = 0.728$

B.3 Mass flux $G = 167$ kg/m^2-s

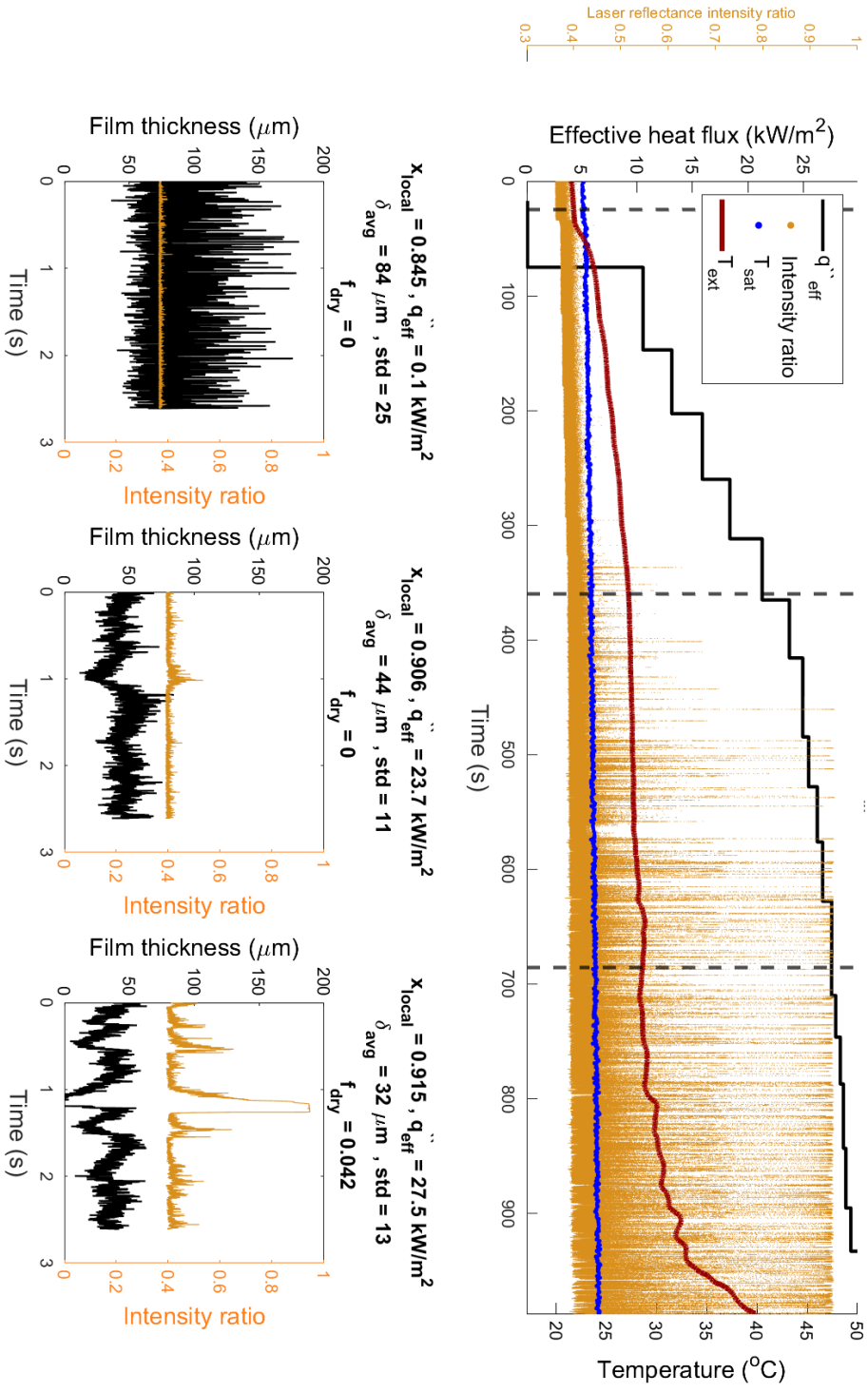

Figure B.4: $G = 167$ kg-m^2-s , $x_{in} = 0.84$

Appendix C

Flow loop interface & control

C.1 Preparing loop for operation

1. **Open valves & turn on power supplies**

   There are a number of valves that must be opened prior to operation of the facility. They are labeled on the schematic sheet. The valves for the city water cooling must also be opened or the heat pumps will not operate properly. Turn on both of the two large power supplies that control the window heating (above the pulse generator).

2. **Open LabView**

   The LabView program is used to operate the loop and also to read/write sensor information into a .csv file. Open the LabView project file from the box folder:

   /box/annularflow/Facility/LabView 2019/LoopRebuild.lvproj

   A window will appear with a list of files contained within the project. Click on the file that says: '*2019RefLoopPulseGen.vi*'. Click run (little white arrow) and the settings window will appear. A view of the LabView program is shown in Figure C.1.

3. **Enter safety settings**

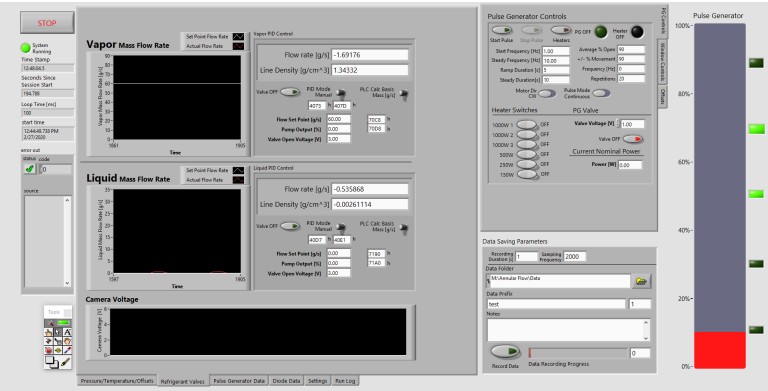

Figure C.1: View of the LabView program

The settings windows are Input, Output, Safety and Other Functions[1]. Click on the Safety tab show the safety settings as seen in Figure C.2. The safety settings are in place to turn off the heating power to the pulse generator and/or windows. This is meant to prevent temperatures and pressures within the loop reaching magnitudes of which are greater than the designed conditions.

By default the **Pulse Generator** settings are:

$$P_{max} = 250 \text{ kPa}$$

$$T_{max} = 35\ ^{o}\text{C}$$

$$t_{\text{at max}} = 60 \text{ sec}$$

The default safety setting for the **Window heaters** is: $\dot{m}_{min} = 1$ g/s.

Please do not change these settings [2]. Click the button that says COMMIT SETTINGS.

4. **Save no offset file**

After committing to the settings, will LabView start to take measurements and display

[1]Poetic, am I right?
[2]Only Jason & Roman will do this.

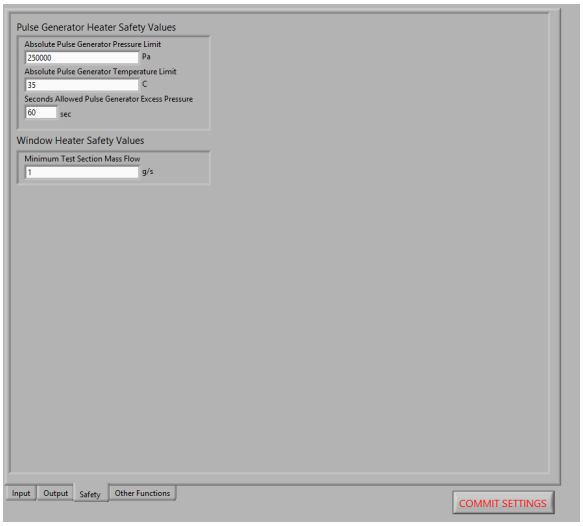

Figure C.2: The safety settings screen within the LabView program

some of them the plots. On the bottom right of the LabView program is a box labeled **Data Saving Parameters**, as seen in Figure C.3. Click on the button labeled with a yellow folder to designate where the files will be saved. Navigate to the folder labeled,

mfval(//nas1.cae.wisc.edu)(M:)/Annular Flow/Data/

Create a new folder and label it using the current date in the format of '**2020-M-D/**', where M is the month number and D is the day number. Within the new folder, create another folder labeled '**CSV**'. The directory displayed in the Data Folder window should be:

M:/Annular Flow/Data/2020-M-D/CSV

Change the name of the data file to **'nooffsets'**. Change the recording time to 60 seconds and click the green Save Data button.

5. **Set offsets - pt. 1**

   Before data is collected, the signal from each pressure transducers is lightly calibrated against corresponding thermocouples (many of which have been calibrated in a water bath). With all the valves open, the loop becomes one large saturated refrigerant

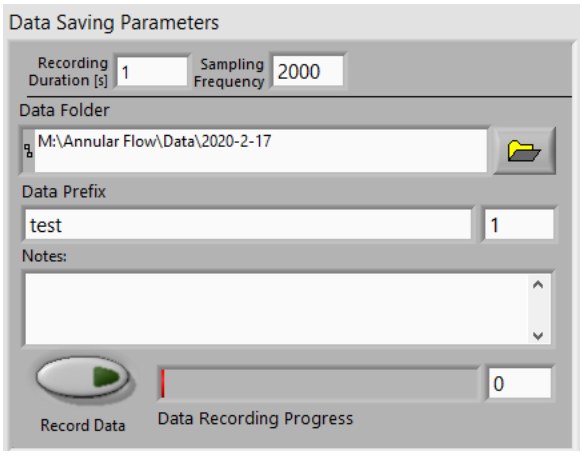

Figure C.3: The Data Saving Parameters window within the LabView program.

container. All temperatures within the loop should be nearly identical to the ambient temperature. Given that we know the temperature of the saturated mixture, we then also know the pressure at each location in the loop.

Navigate to the window labeled **Pressure/Temperature/Offsets**, the first tab on the bottom left of the program, as seen in Figure C.4. By clicking the 'AUTO OFFSET' button each of the pressure transducers is given an offset such that the measured pressure is equal to the saturation pressure.

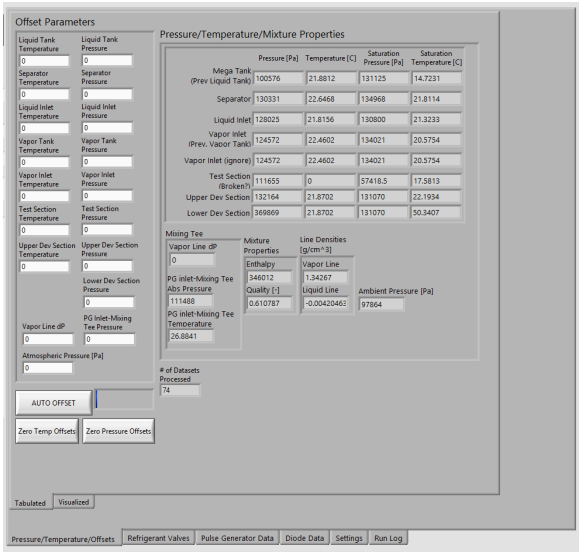

Figure C.4: Temperature and pressure measurements and location of first offset

6. **Set offsets - pt. 2**

   The differential pressure transducers installed in the test section must also be offset. When there is no flow, the measured differential pressure should be equal to:

$$\Delta P = \rho g h$$

   where ρ is the density of R-245fa vapor, g is gravitational acceleration and h is the elevation difference between the two pressure ports. The value of h depends on which of the pressure ports are open to the test section. Currently we are taking measurements between locations marked 1 and 3 on the schematic of the pressure line array. The difference in elevation for this case is $h = .375$ m. Use EES Klein (2019) to get the density of the vapor and to make the calculation for ΔP.

   Navigate to the window labeled **Pulse Generator Data** and find the window labeled **Pulse Generator Offsets** as shown in Figure C.5. In the LabView program find readings of $\mathbf{W17\ dP_{fast}}$ and **W17 dP**. Enter an offset for both transducers so the reading now matches the calculated ΔP.

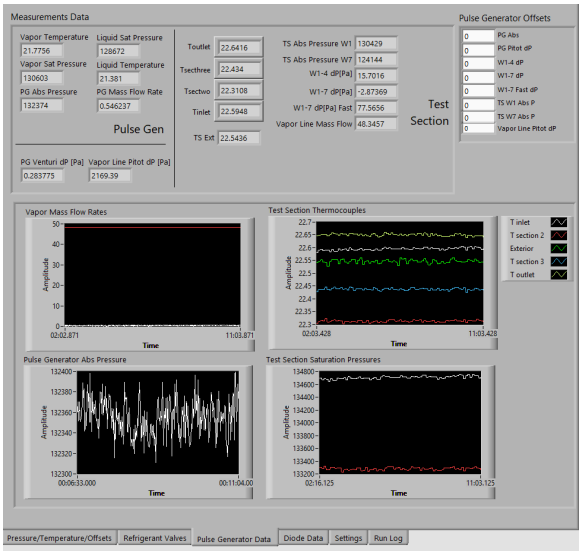

Figure C.5: Pulse Generator Data screen and location of differential pressure offsets.

7. **Save offset file**

With the offsets in place, change the name of the data file to **'offsets'**. Push the Save Data button and record another 60 seconds of data. We are now ready to fire up the loop.

C.2 Flow loop launch sequence

1. **Close bypass**

   Prior to starting pumps, close the bypass valves between the separator and storage tank[3]. Liquid refrigerant may begin moving in the line from the outlet of the condenser to the storage tank. This is normal.

2. **Turn on water/glycol loop**

   The water and propylene glycol loop is what provides the heating power and cooling power necessary to vaporize and condense the refrigerant within the annular flow loop. The startup for the water/glycol loop can be summarized in a only a few steps:

   (a) Check the temperature controllers by the LabView PC. The set points for the hot and cold side are $\sim 42\ ^o$C and $\sim 10\ ^o$C. Please do not change these temperatures[4]

   (b) Double-check that the city water valves are open.

   (c) Turn on secondary pumps (small pumps).

   (d) Turn on primary pumps.

   (e) Turn on heat pumps.

   (f) Wait. It will take a few minutes for the heat pumps to bring the water/glycol mixture to the set temperatures. Be patient and check the temperature controllers periodically.

   If after some time either the hot or cold side is unable to reach the desired temperature, then it is likely that the city water valve is not opened properly. If this occurs and the city water valve has been properly opened, then it is likely that the heat pumps are not receiving electrical power. Check the heat pump switches and then the breaker

[3] Also known as MegaTank.

[4] Again, Jason and Roman have omnipotent power in this domain.

box if necessary. If the valve is open, the heat pumps appear to be running correctly and the temperatures of the water/glycol still do not reach the desired set point, turn off heat pumps and contact the nearest graduate student.

C.3 Mass flow control

The annular flow facility is capable of running solely vapor, solely liquid and saturated flows. The annular flow regime is observed in flows with high vapor qualities[5]. Vapor and liquid mass flow rates are controlled by separate gear pumps, and each posses a control valve upstream of the location at which they are injected into the flow loop. Mass flow rates are measured by Coriolis flow meters just downstream of each of the pumps. Figure C.6 displays the panel within the LabView program that is used to control mass flow rates.

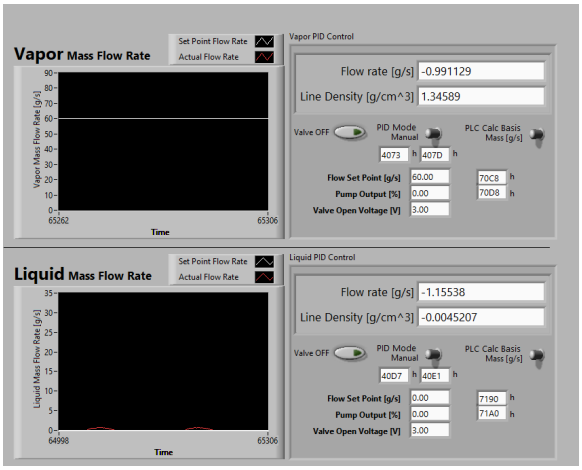

Figure C.6: Vapor and liquid mass flow rate control panel

C.3.1 PID control

The frequency at which the gear pump operates is varied to maintain the desired flow rate for each liquid and vapor. Based on the mass flow measurement, the pump either speeds up or slows down to overcome pressure oscillations within the loop that would otherwise disrupt the steady flow of mass. The pumps are controlled with a proportional-integral-derivative (PID) controller tied in seamlessly to work within the LabView program[6].

[5] $X > .5$ is a good place start for this experiment. The regime actually depends on both quality and total mass flux.

[6] Using mostly magic.

C.3.2 Manual control

The same as PID, except now the user is the PID. Flow rates will need to be controlled by adjusting the output of the pumps and the valve voltages.

C.4 Operation

The general steps for introducing vapor and liquid mass into the flow loop are:

1. **Introduce vapor**

   Click the green button labeled **Valve** that lies to the right of the vapor mass flow rate. The button should light up and the indicator will change from OFF to ON. Ensure there is liquid refrigerant inside of the tubing at the pump inlet. It may be necessary to wait a few minutes while gravity and capillary effects draw liquid to the inlet of the pump. Turn the pump on by increasing the pump output to ∼25%. There may be some bubbles that come out of the pump for the first few moment, but this should cease quickly. Once ensured that the pump is not going to run dry, switch the control from manual to PID and change the vapor mass flow rate to the desired amount (∼45 g/s is a good starting flow rate for vapor). Adjust the valve voltage between 3-4 volts such that the pumps output is around 55% [7].

2. **Introduce liquid**

   Once vapor flow has appeared to stabilize, turn the liquid pump on by increasing the output to ∼30%. Open the liquid control valve by clicking the green button. This will introduce liquid into the flow loop. After a brief moment when the liquid flow rate has appeared somewhat stabilize, switch control over to PID mode. Set the desired liquid flow rate (∼12 g/s is a good starting flow rate for liquid). Finally, adjust the valve voltage such that the pump output is around 55%.

[7] Based on experience, the mass flow is more consistent when the pump is operating at a base level greater than 50%.

3. **Instability**

   For low vapor qualities, large oscillations in pressure and temperature are recorded in the test section. The amplitude of the temperature oscillations can be as large as +/- 1 ^{o}C in the test section, and the pressure oscillations can be as large as +/- 5 kPa. These oscillations are too large to get any meaningful steady state data and so this regime is to be avoided. Increasing the vapor flow rate and/or decreasing the liquid flow rate is usually enough to exit this regime and enter a regime of stability. If the oscillations continue to occur at high vapor qualities, the difference in temperature between the hot and cold sides of the loop may be too large. Consult a graduate student.

C.5 Window heating control

The windows are coated with fluorine-doped tin oxide (FTO). This allows for heating at the surface by way of ohmic dissipation. Each window has a power supply that has been integrated into the LabView program. The window heater control panel is seen in Figure C.7. The green button in the upper left hand side of the panel is the ON/OFF button. When the red safety trigger light is on, the LabView program will refrain from providing power to the windows. The *Saftey Trigger* comes on if the safety settings that were put into place when the LabView was launched are not met.

If the red indicator light is not on, then you will be able to provide current to the windows. To turn the window heaters on, press the green button. Change the power setting for each window to the desired window heating power. If the desired power is unable to be met due to current or voltage limits, change the limits on voltage and/or current to increase the overall power limit.

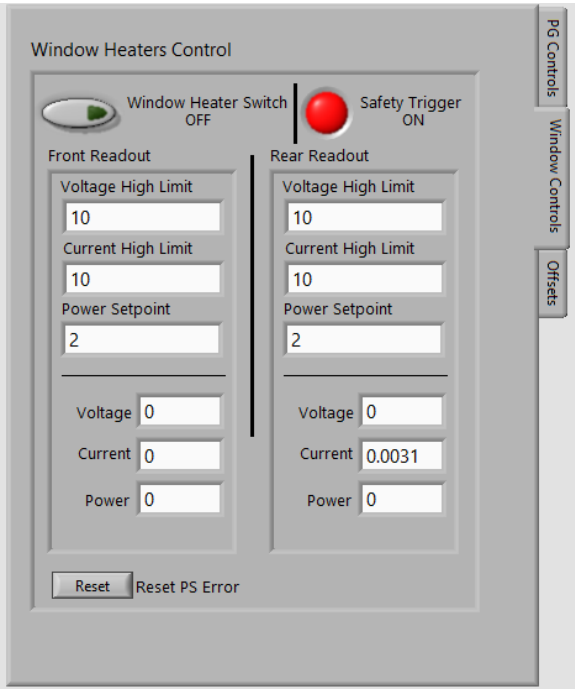

Figure C.7: Window heating control window

C.6 Pulse Generator control

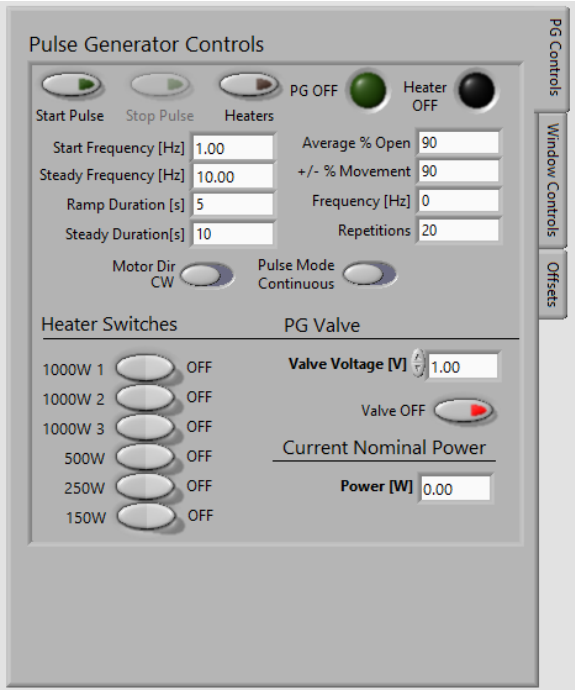

Figure C.8: Pulse generator control window

The pulse generator adds vapor pulse injections at a desired frequency. The tank is pressurized by heating to increase the temperature and therefore the saturation pressure. The heating elements in the tank are rated for different powers and they can be used in any combination allowing. Changing the heating power provided to the tank changes the rate at which refrigerant is vaporized and therefore changes the amplitude of the vapor pulses. The vapor pulses are introduced into the loop by opening and closing a 3 inch ball valve just downstream of the saturated tank. The valve is opened by a stepper motor and controlled via LabView. Mass flow from the pulse generator is measured using a Venturi flow meter downstream of the ball valve. The control panel for the pulse generator can be seen in Figure C.8. In the upper left hand corner of the panel is the *Start Pulse*, *Stop Pulse* and *Heaters buttons*. The stepper motor ramps up to the desired frequency in order to avoid large amounts of torque on the motor. The *Start Frequency* is the frequency at which the stepper motor will begin and the *Steady Frequency* is desired frequency for the data run. On the bottom of Figure C.8 the ON/OFF buttons for individual heaters within the pulse generator can be seen. Activating all 6 heaters will provide 3900 W of nominal heating power. The liquid inside of the pulse generator is refilled by opening a valve between one of the pumps and the pulse generator.

A quick list of safety guidelines for the pulse generator:

1. If the heaters are on, pay attention to the absolute pressure inside of the pulse generator. Increasing pressure within a closed container is dangerous.

2. If the sound of grinding accompanies the onset of the pulsing, click *Stop Pulse*. It is likely that the stepper motor was not provided with enough time to ramp up.

3. Keep an eye on the liquid level within the tank. On the right hand side of the LabView program there is a large display that indicates the level of the tank based on float switches mounted in the tank. If the tank becomes dry and the heaters remain on the

heating elements will likely be damaged.

Congratulations! You have successfully wrangled the beast.

Now, we science.